에너지 저장 소재 설계
Design of Energy Storage Materials

Uk Sim, Ph. D.

Nanomaterials for Energy & Environment Laboratory
www.uksim.org

Nitrogen and Fluorine co-doping in Graphene Quantum Dot

Applied Surface Science, 2020, 511: 145424

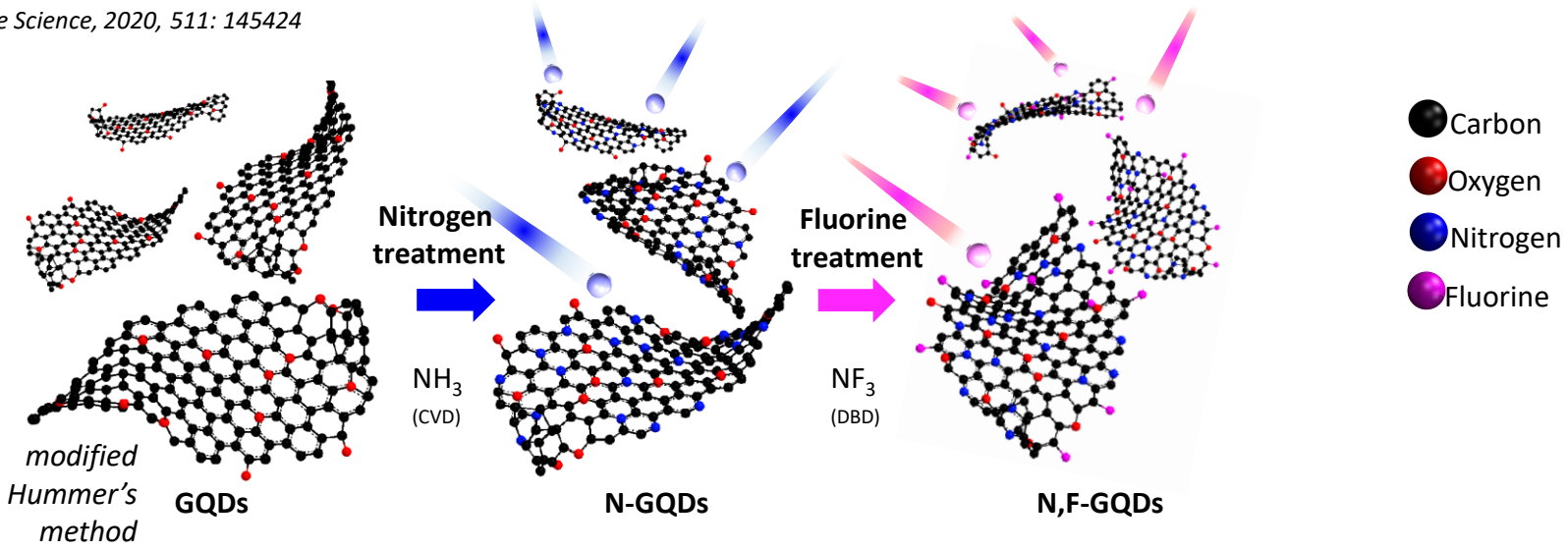

AFM images of the GQDs dispersed on a SiO_2 substrate

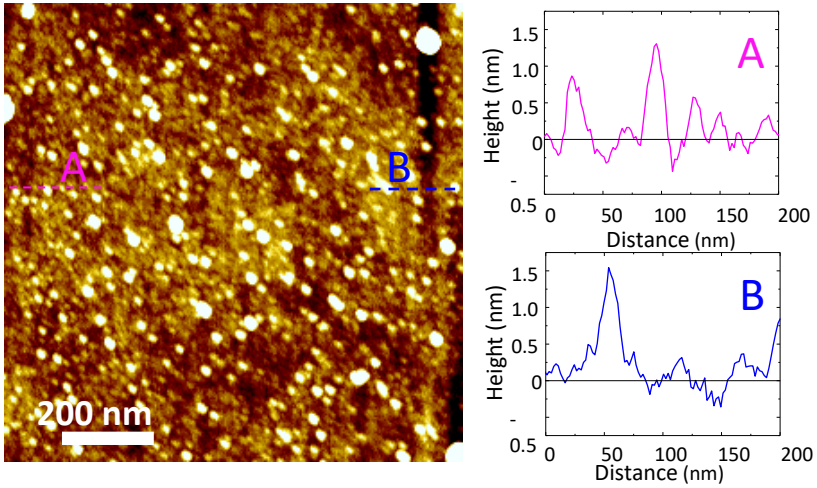

- An average height is under 1.5 nm height, which indicates the number of layers in N,F-GQDs were about ~3 layers

TEM image of GQDs

TEM grid was supported by monolayer graphene grown by CVD

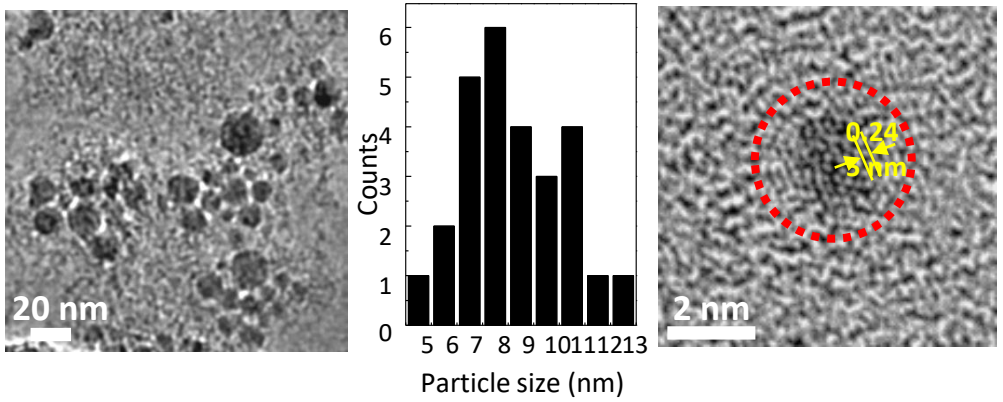

- An Most of N,F-GQDs dispersed on graphene sheet show a size distribution from 2 to 10 nm with an average size of 8.7 nm.
- TEM image indicates the N,F-GQDs are highly crystalline

Nitrogen and Fluorine co-doping in Graphene Quantum Dot

Applied Surface Science, 2020, 507: 145157.

X-ray photoelectron spectroscopy (XPS)

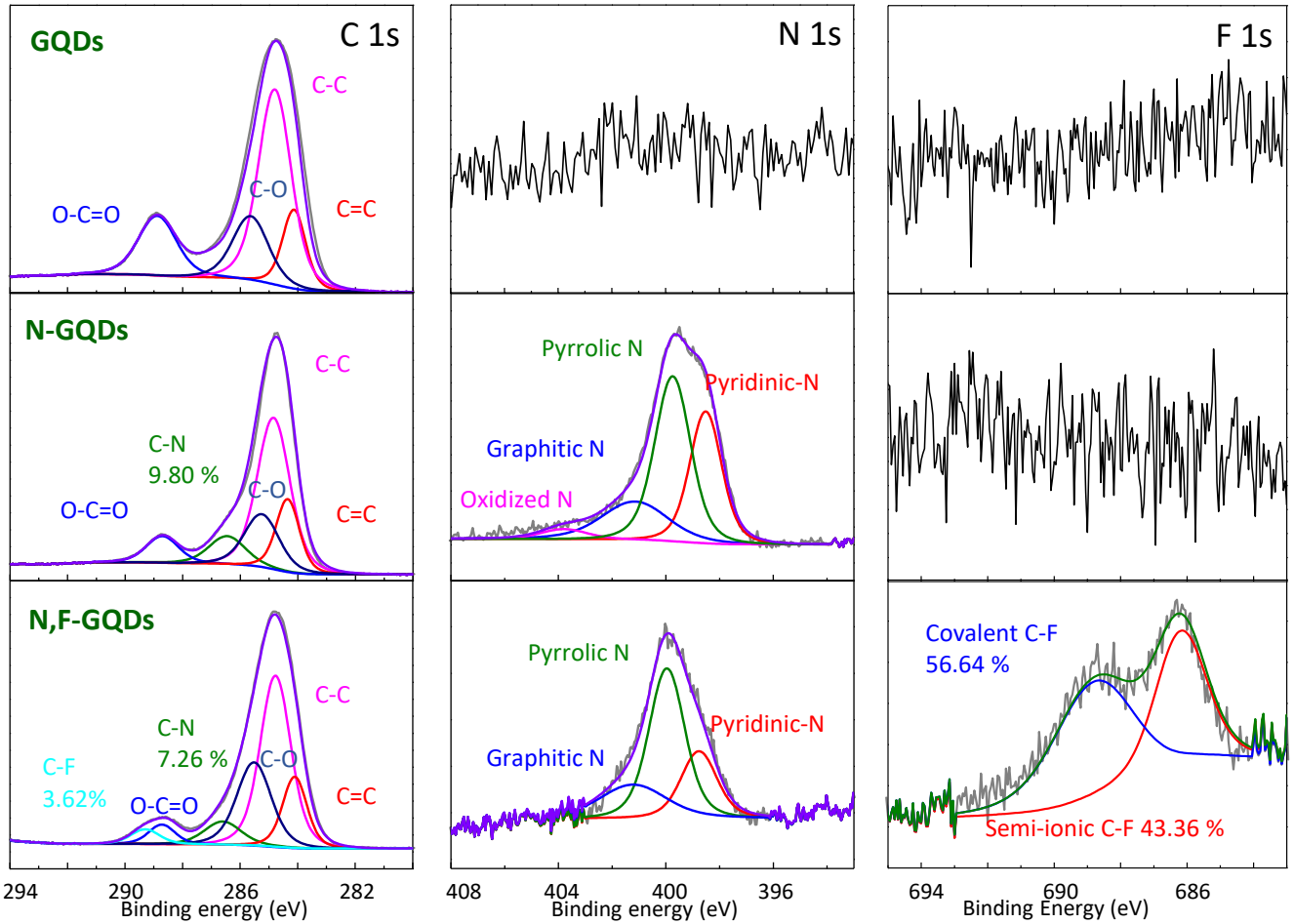

FT-IR

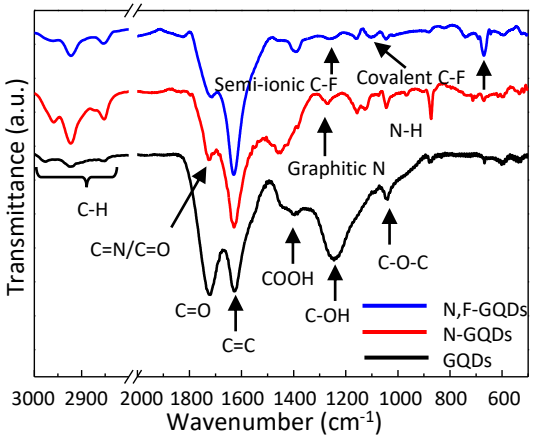

C-F bond is consisted of covalent C-F bond (688. 8 eV) and semi-ionic C-F bond (686.2 eV)

- N-GQDs and N,F-GQDs show that the peak at 286.4 eV attributed to C-N bond appears whereas the intensity of carboxyl bonding at 289.0 eV is relatively decreased → Nitrogen and fluorine substitute oxygen
- N 1s peak of N-GQDs and N,F-GQDs exhibits three peaks at 398.5 (pyridinic N), 399.8 (pyrrolicN), and 401.1 eV (graphitic N), respectively, which nitrogen is successfully functionalized on N-GQD and N,F-GQDs

Nitrogen and Fluorine co-doping in Graphene Quantum Dot

Applied Surface Science, 2020, 507: 145157.

3-electrode capacitance measurement as positive electrode

Capacitance of N,F-GQDs ; 244.46 F/g @ 3 mA/cm^2

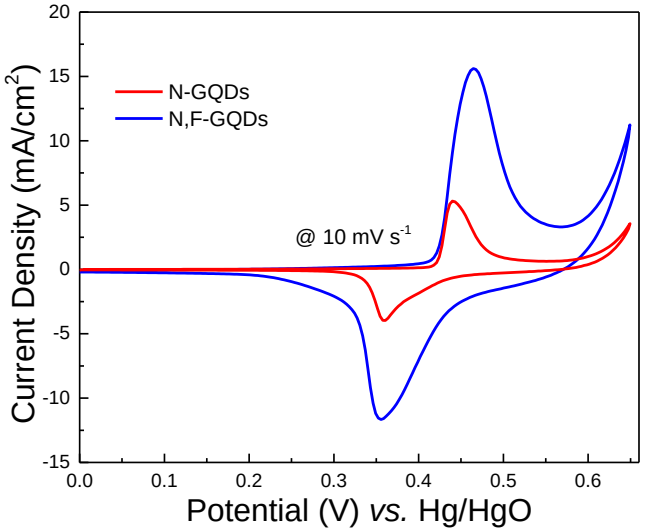

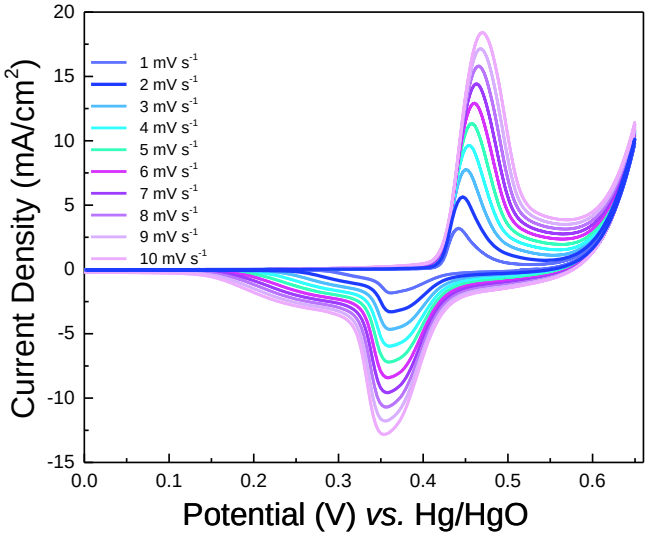

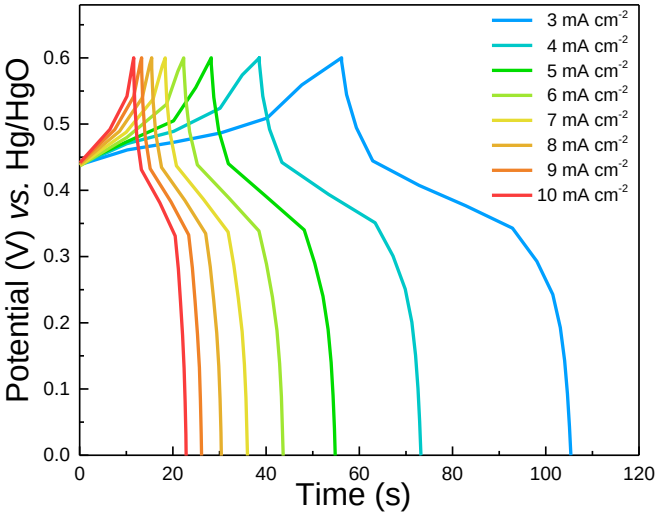

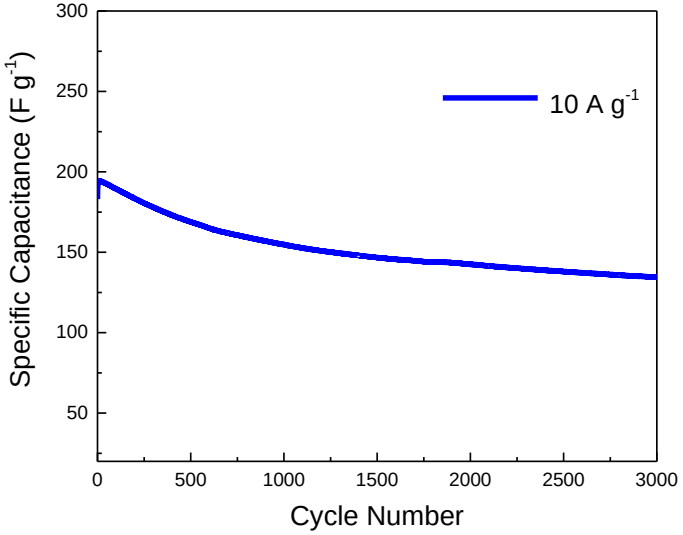

- carbon-based materials have the ability to charge and discharge quickly and long cycle life due to the physical adsorption and desorption of electrolyte ions without the chemical reactions
- high electronegativity difference between fluorine and nitrogen-doped carbon generates positively charged carbons which accelerating the capacitance toward positive potential range

Asymmetric Supercapacitor using Fe_3O_4 and Ni_2P

Applied Surface Science, 2020, 507: 145157.

XRD of Fe_3O_4 and Ni_2P

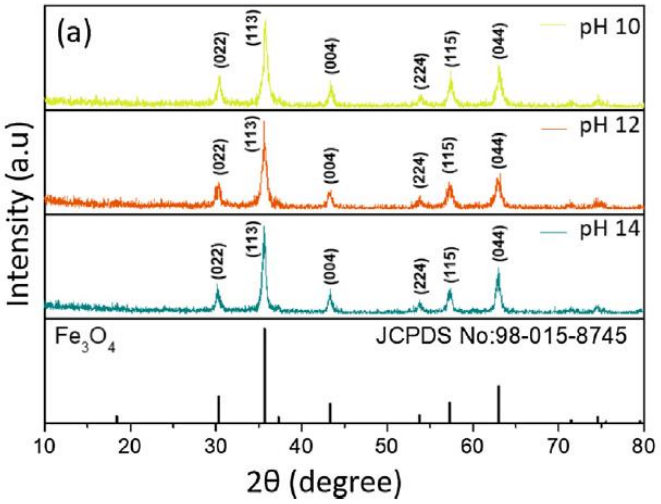

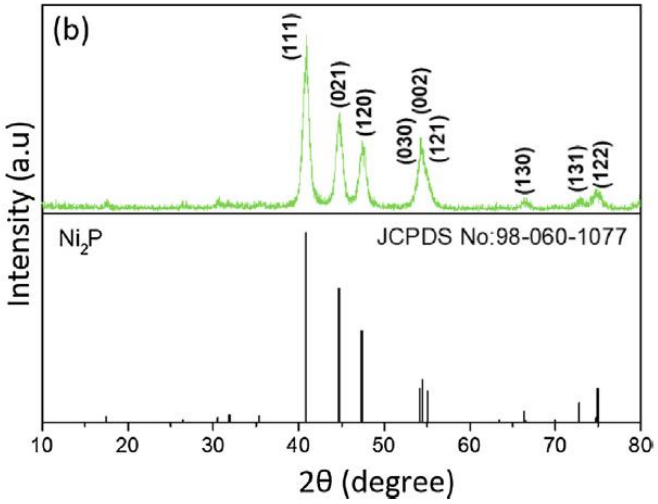

- The XRD pattern with strong peaks reveals the single phase formation of highly crystalline Fe_3O_4 and Ni_2P nanoparticles with the cubic and hexagonal crystal structure.

XPS of Fe_3O_4 and Ni_2P

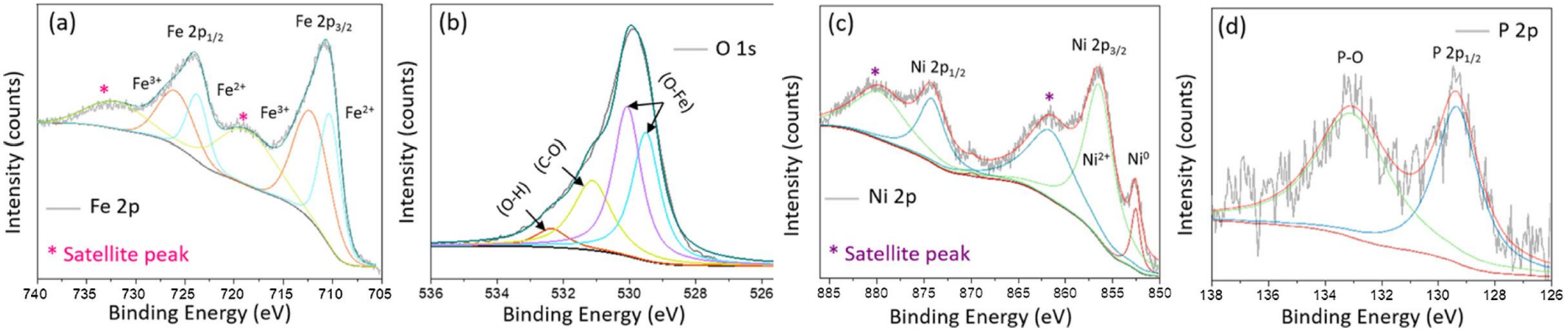

- This affirms the transfer of an electron from Ni to P in the prepared Ni_2P.
- The single-phase formation and surface composition of Fe_3O_4 and Ni_2P were confirmed by XPS analysis.

Asymmetric Supercapacitor using Fe_3O_4 and Ni_2P

Applied Surface Science, 2020, 507: 145157.

SEM, TEM, and EDS mapping of Ni_2P

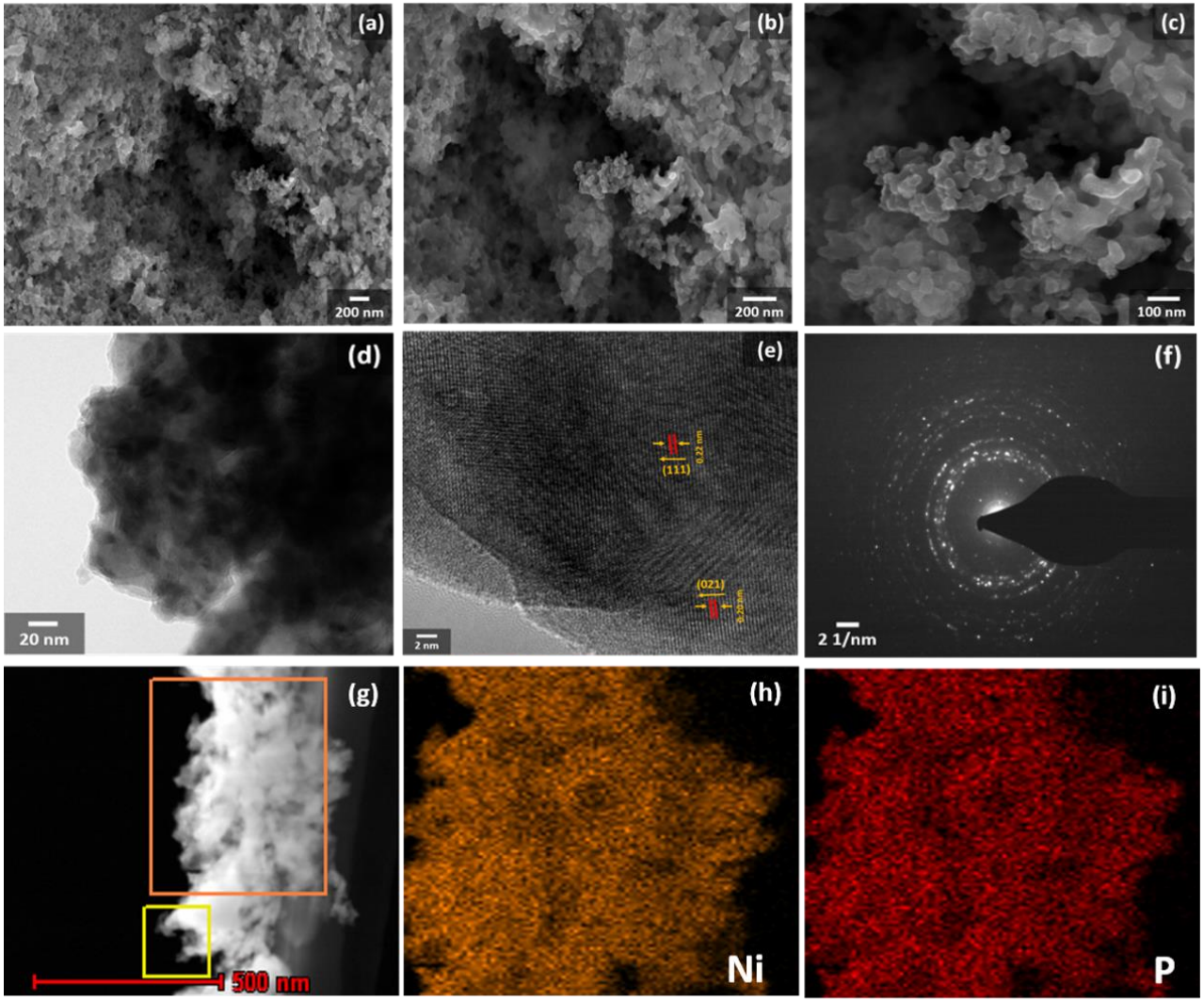

- The FESEM images reveals the uniformly distributed spherical nanoparticles of Fe_3O_4. The interconnected spherical particles influence more vacant space that can facilitate the improved absorption rate of electrolytic ions during electrochemical activity.
- The HRTEM images clearly visualizes the noticeable crystal lattice with an interplanar spacing value of 0.25 and 0.29 nm that is equivalent to the d-spacings of (1 1 3) and (0 2 2) crystal plane of cubic Fe_3O_4.

Asymmetric Supercapacitor using Fe_3O_4 and Ni_2P

Applied Surface Science, 2020, 507: 145157.

SEM, TEM, and EDS mapping of Fe_3O_4

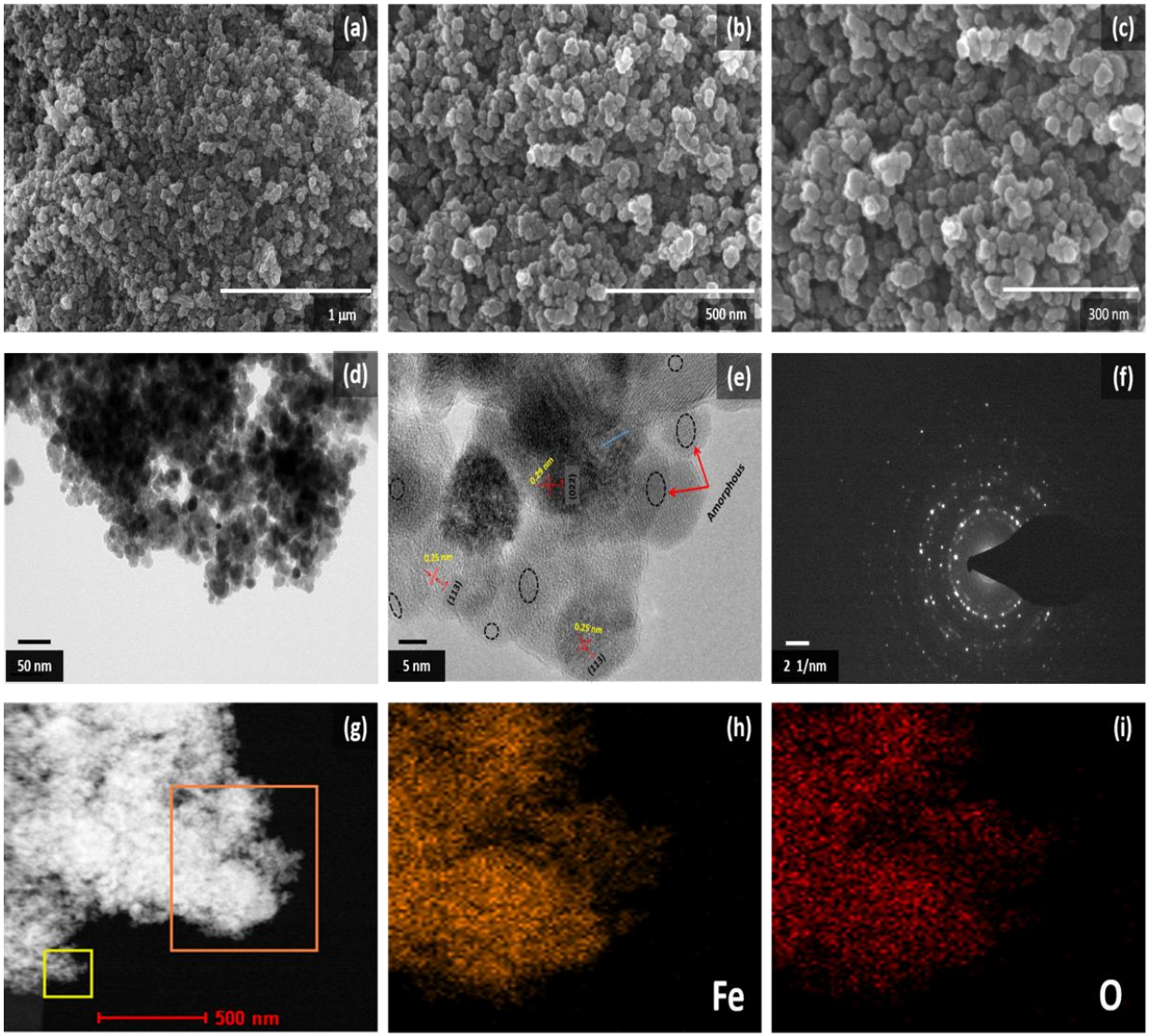

- the FESEM images of Ni_2P reveals uniformly distributed clusters of globular nanoparticles. The particle size of the nanomaterial was estimated to be around 20 nm. These Ni_2P nanoparticles are linked together, forming web-like clusters that can suitably absorb the enormous number of electrolytic ions.
- the HRTEM image of Ni_2P nanoparticles illustrating well-defined fringes with appropriate interplanar spacings of 0.22 and 0.20 nm, with respect to the d-spacings of (1 1 1), and (0 2 1) crystal planes of hexagonal Ni_2P.

Asymmetric Supercapacitor using Fe_3O_4 and Ni_2P

Applied Surface Science, 2020, 507: 145157.

3-electrode half cell test @ negative potential range (Fe_3O_4)

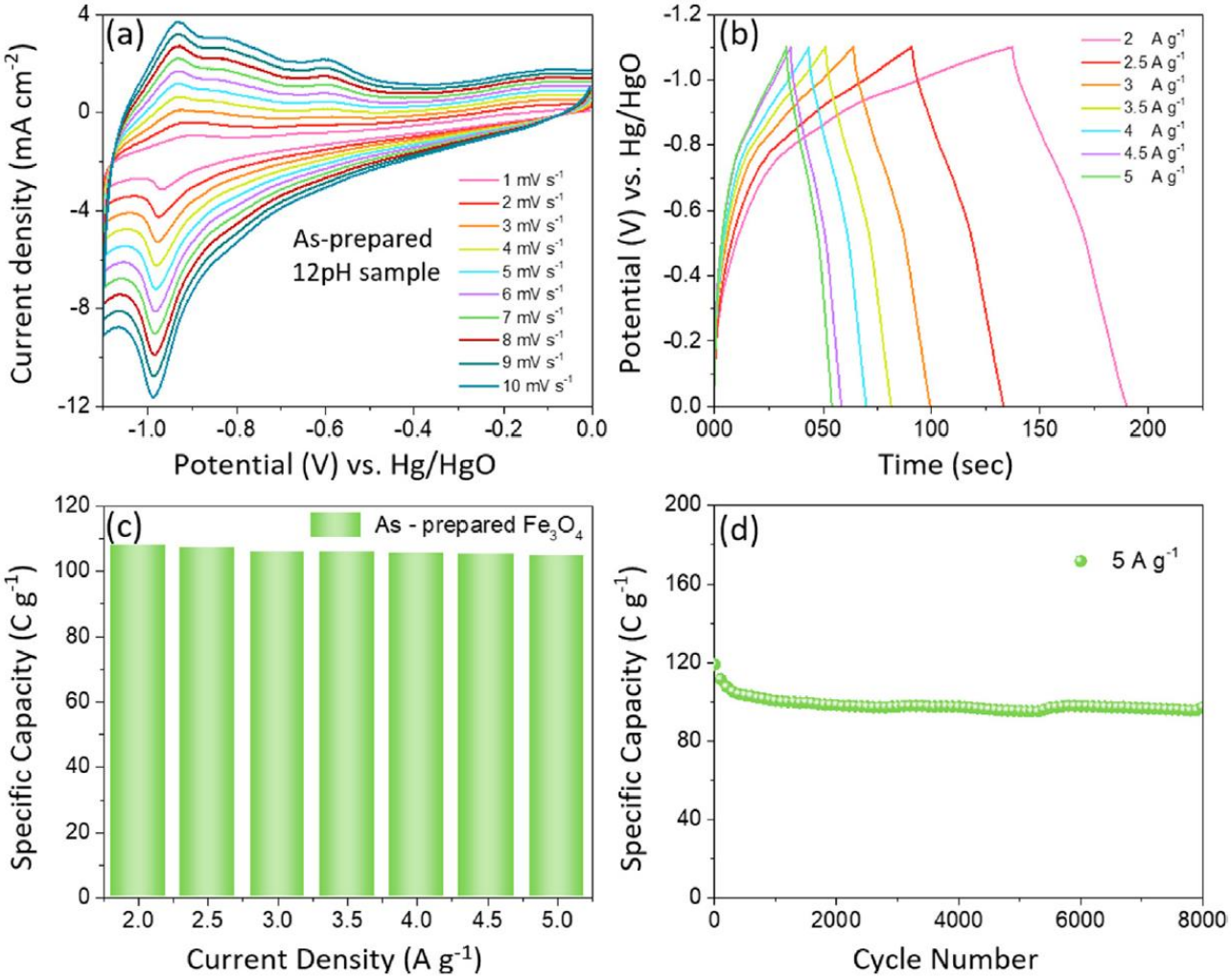

- The observed prominent redox peaks from the CV curves of the Fe_3O_4 electrode suggest the contribution of the Faradaic mechanism. The noticed peaks correspond to the highly reversible oxidation and reduction reactions of Fe^0/Fe^{2+} to Fe^{2+}/Fe^{3+} and Fe^{3+}/Fe^{2+} to Fe^{2+}/Fe^0, respectively.
- From the obtained CV curve, the specific capacity of the Fe_3O_4 was calculated to be 176 C g^{-1} at a scan rate of 1 mV/s.
- The calculated specific capacity of the Fe_3O_4 electrode is 108 C g^{-1} at 2 A g^{-1}.

Asymmetric Supercapacitor using Fe_3O_4 and Ni_2P

Applied Surface Science, 2020, 507: 145157.

3-electrode half cell test @ positive potential range (Ni_2P)

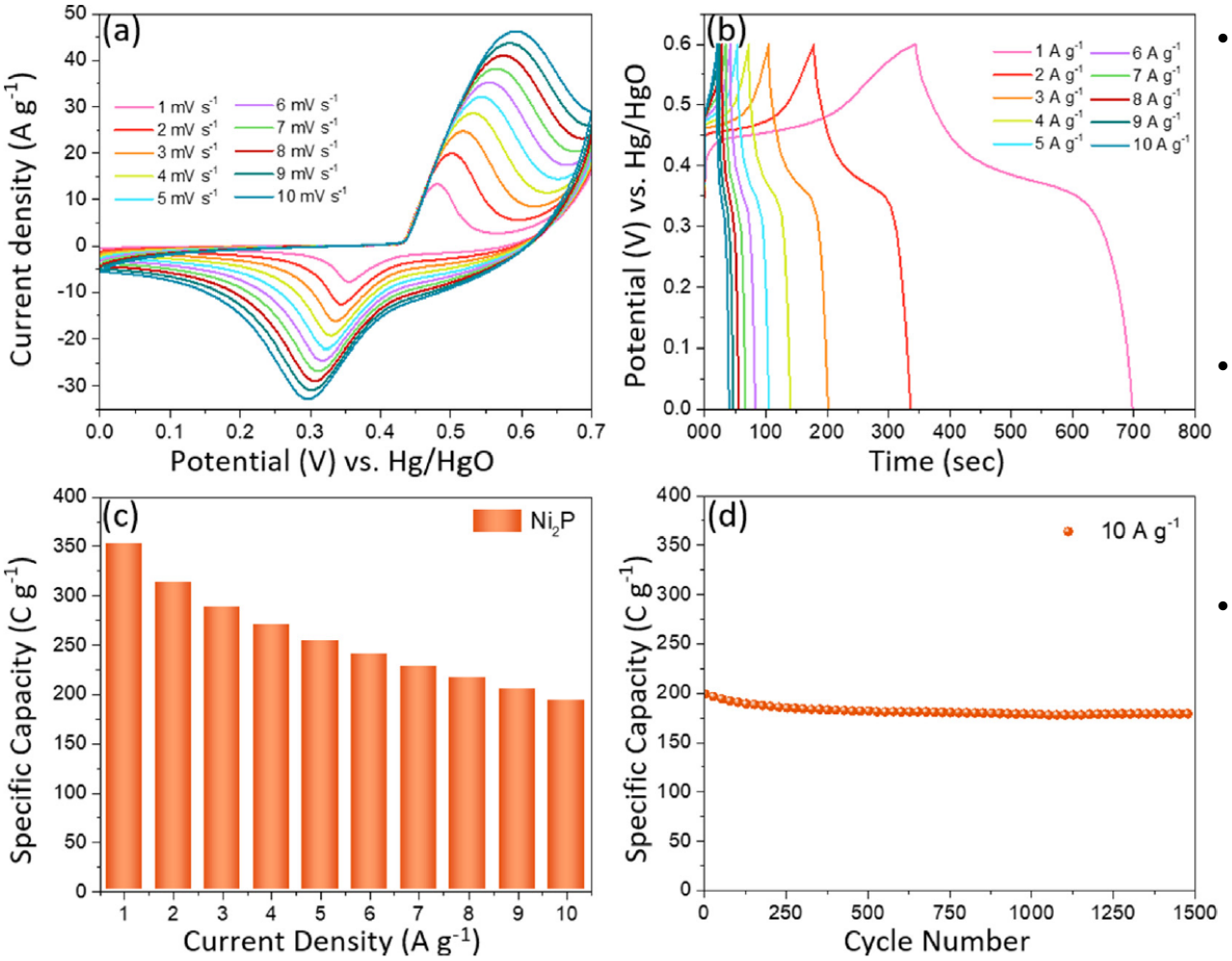

- The redox peaks noted at 0.45/0.4 V (vs. Hg/HgO) affirms the legitimate Faradaic reaction (battery-like) mechanism contributed by the Ni_2P electrode to that initiates charge storage.
- From the obtained CV curve of the prepared Ni_2P, the specific capacity was calculated to be 449 C g^{-1} at a scan rate of 1 mV/s.
- The calculated specific capacity of Ni_2P electrode is 354 C g^{-1} at a current density of 1 A g^{-1}.

Asymmetric Supercapacitor using Fe_3O_4 and Ni_2P

Applied Surface Science, 2020, 507: 145157.

EIS data

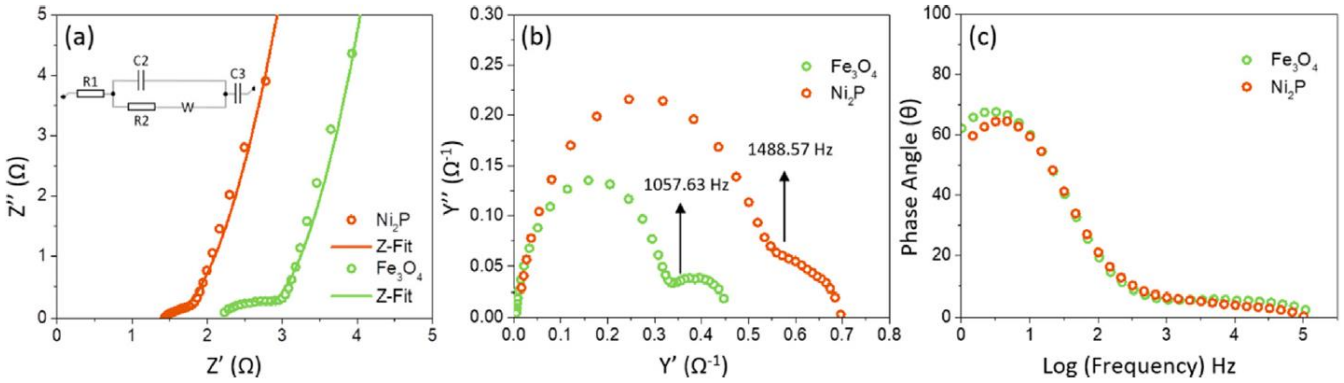

- the prepared Fe_3O_4 and Ni_2P electrodes possess improved conductivity with low charge transfer resistance that promotes superior charge storage property.

2-electrode device test for hybrid supercapacitor

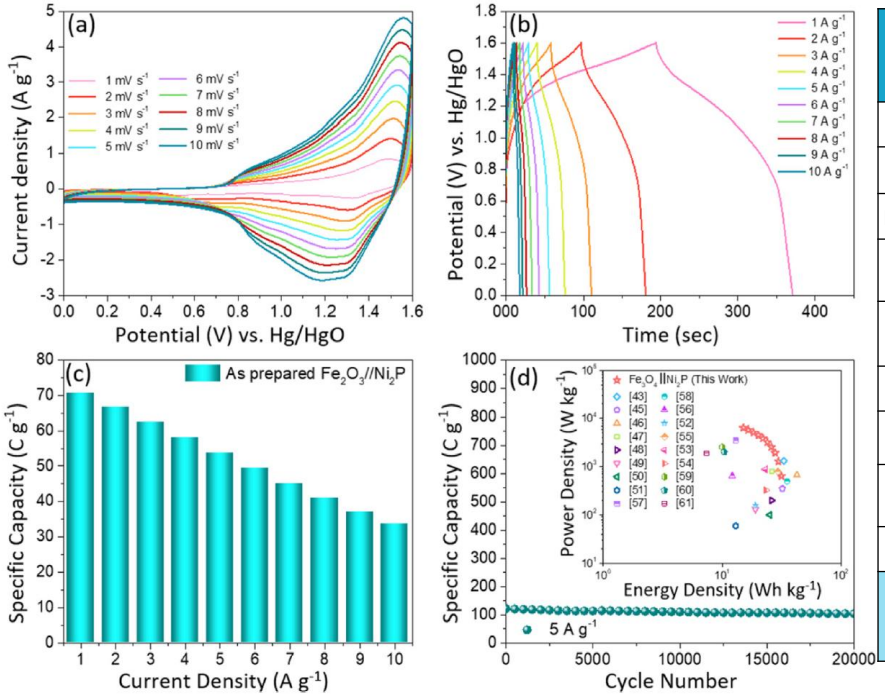

Device materials	Substrate	Electrolyte	Energy Density (Wh kg^{-1})	Power Density (W kg^{-1})
NGPCZ || NGPCZ @MnO_2	carbon	1 M Na_2SO_4	25.93	199.9
MnO_2 || graphene	nickel foam	1 M Na_2SO_4	25.2	100
$Ni(OH)_2/MoS_2$ || graphene	nickel foam	6 M KOH	13	3500
$CoFe_2O_4$ || rGO	stainless steel	1 M KOH	12.14	643
Fe_2O_3 || $NiCo_2O_4$/NiO	nickel foam	1 M KOH	19	157
$NiCo_2O_4$@$Ni_{0.85}Se$ || AC	nickel foam	1 M KOH	29.3	799
$NiFe_2O_4$/CNT || graphene	nickel foam	2 M KOH	23	872
graphene-MnO_2 || graphene	nickel mesh	1 M Na_2SO_4	10.03	2530
Ni-Co oxide || AC	nickel foam	1 M KOH	7.4	1900
Fe_3O_4 || Ni_2P	Carbon cloth	1 M KOH	31	6400

Fluorine-doped Graphene Oxide for Hybrid Supercapacitor

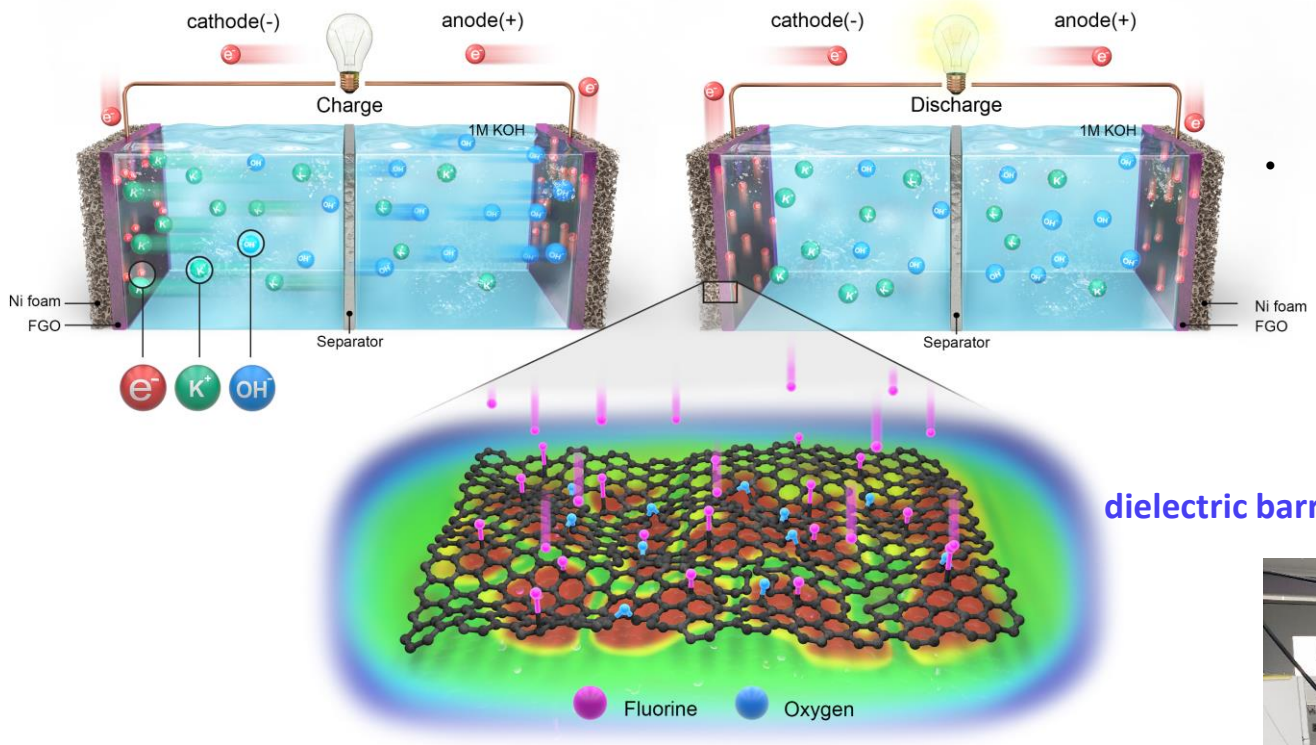

- We firstly introduce a facile methode to synthesize fluorine-doped graphene oxide (FGO) from GO using a direct plasma treatment method that is mass-production compatible at once.
- FGO is applied as cathode and anode at hybrid supercapacitor.

dielectric barrier discharge (DBD) plasma reactor

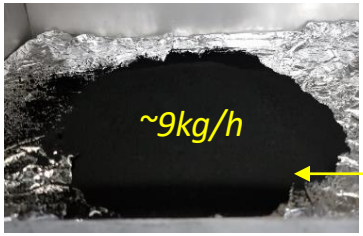

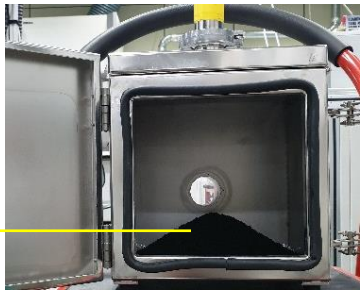

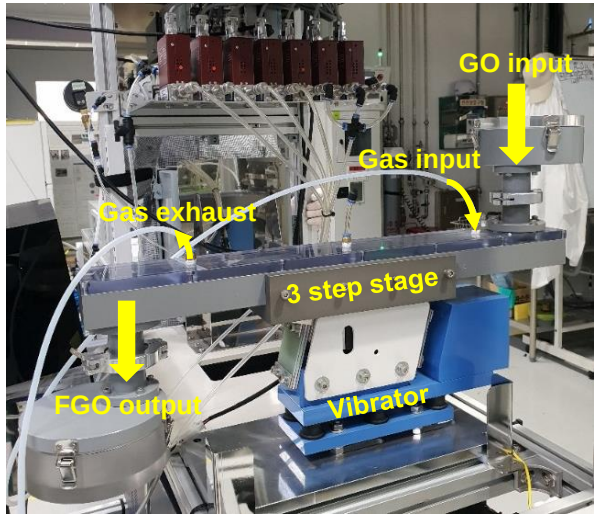

Fluorine-doped Graphene Oxide for Hybrid Supercapacitor

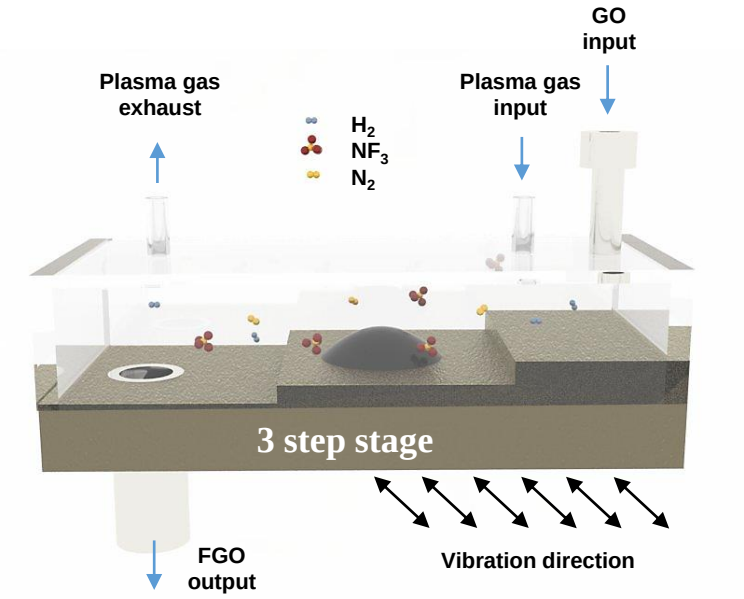

- Graphene was functionalized with fluorine in a dielectric barrier discharge (DBD) plasma reactor using NF_3 source
- peak at 288.5 eV is assigned to C-F bonding
- With increasing F/C ratio, the C-F bonds change their character from ionic to semi-ionic to covalent one and the prepared FGO shows below 4% F/C ration, which inidcates semi-ionic bonding.
- The semi-ionic C-F bonding could enhance the electrical properties of the electrode and facilitate electron transport through the active material.

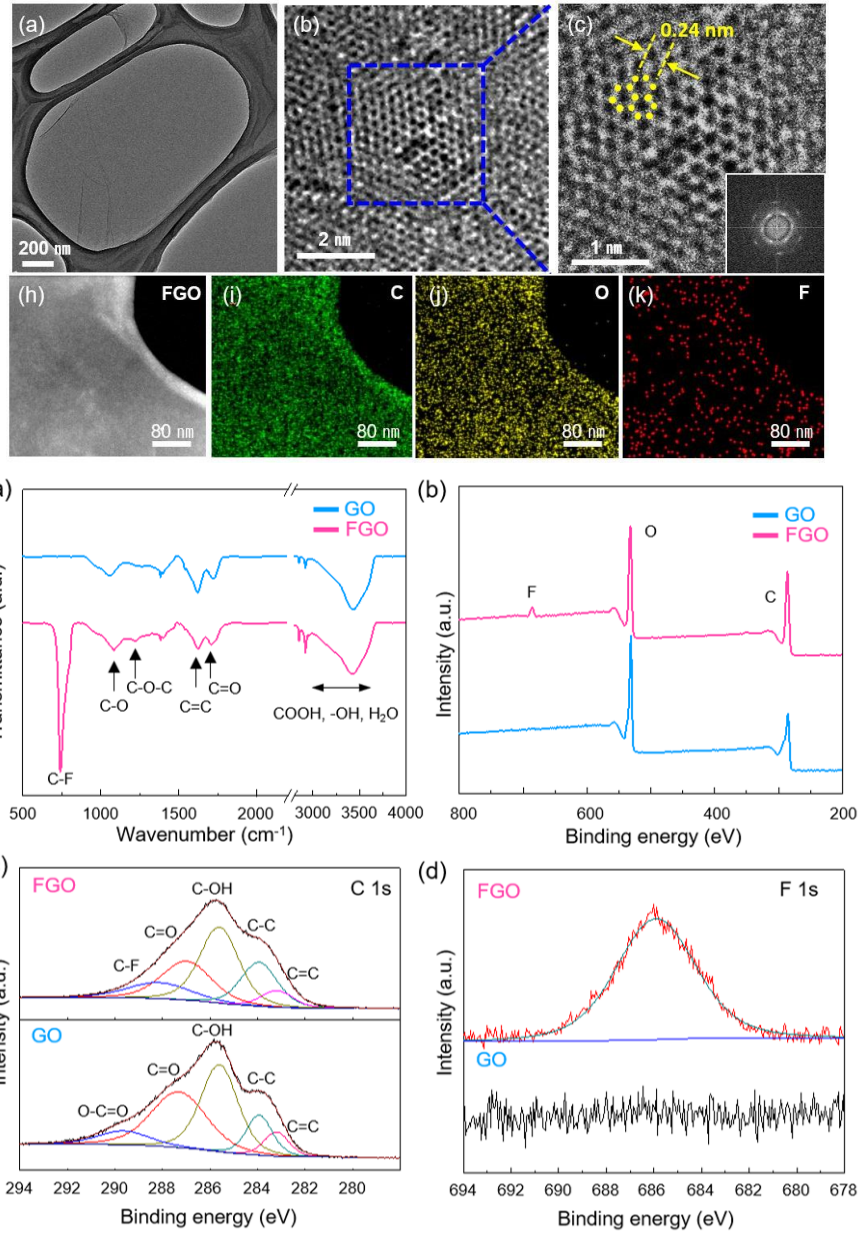

Fluorine-doped Graphene Oxide for Hybrid Supercapacitor

3-electrode half cell test @ negative potential range

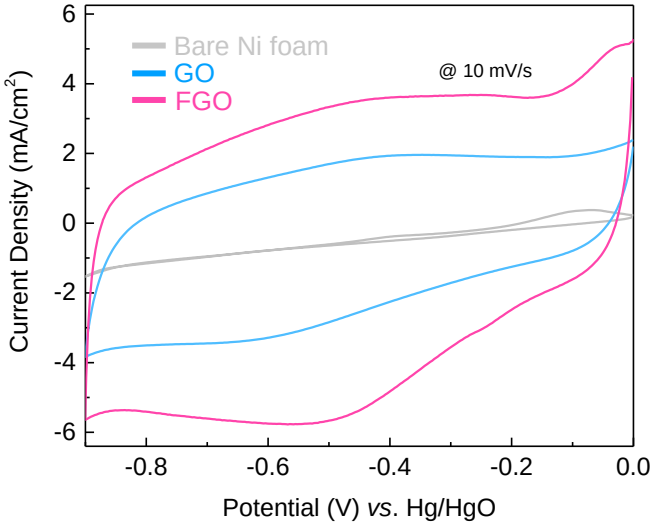

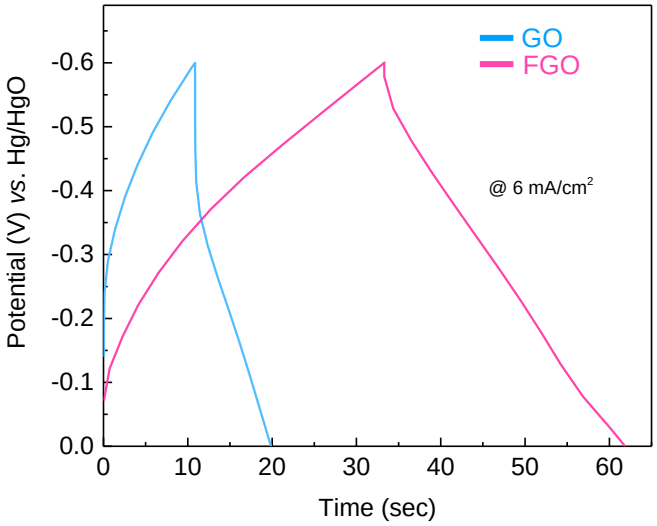

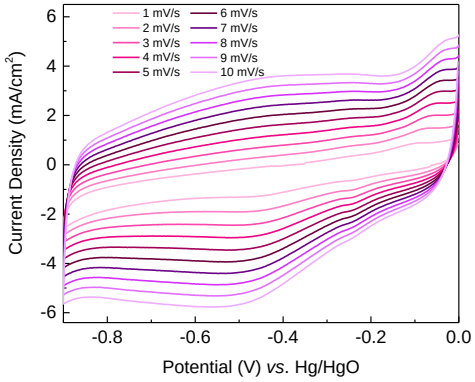

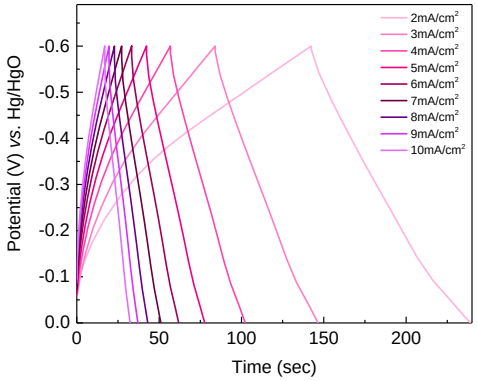

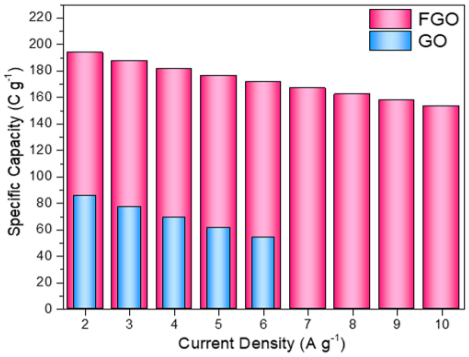

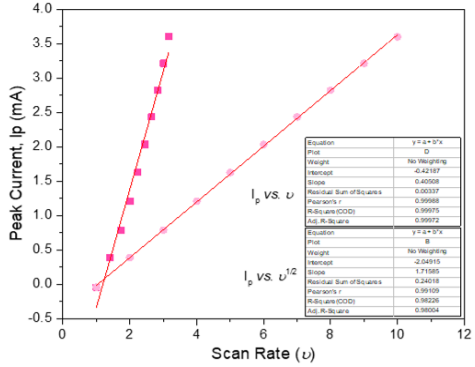

- In negative potential range, FGO exhibits specific capacitance of 294 F/g @ 5mA/cm^2 and shows EDL capacitance behavior.
- Our results indicate that FGO is suitable as cathode and anode for hybrid supercapacitor device.

Fluorine-doped Graphene Oxide for Hybrid Supercapacitor

3-electrode half cell test @ positive potential range

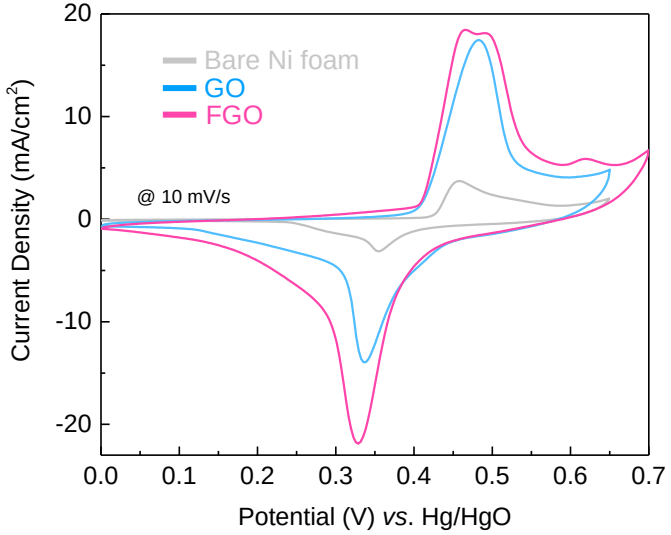

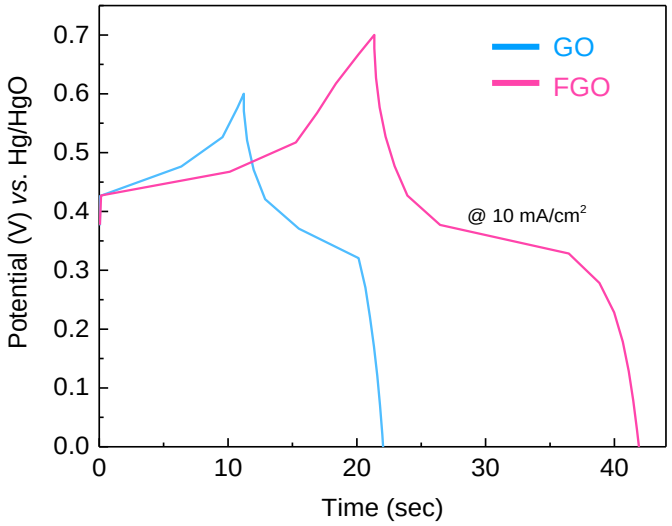

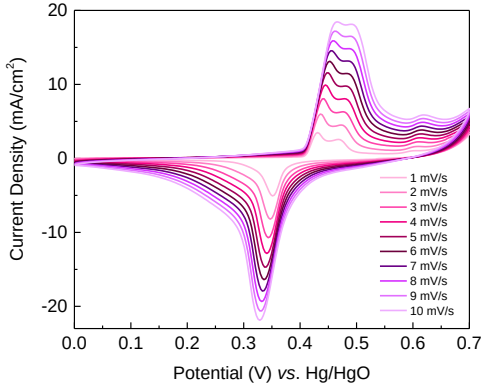

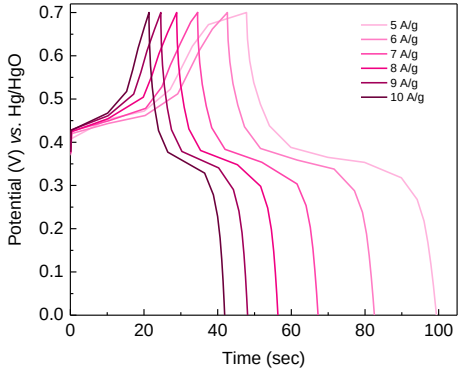

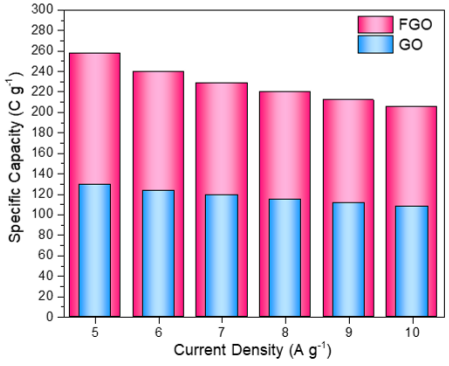

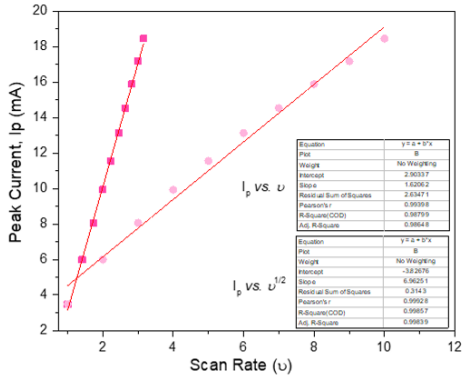

- In positive potential range, FGO exhibits specific capacitance of 368 F/g @ 5mA/cm^2 and shows pseudo capacitance behavior.

Fluorine-doped Graphene Oxide for Hybrid Supercapacitor

Electron localization function

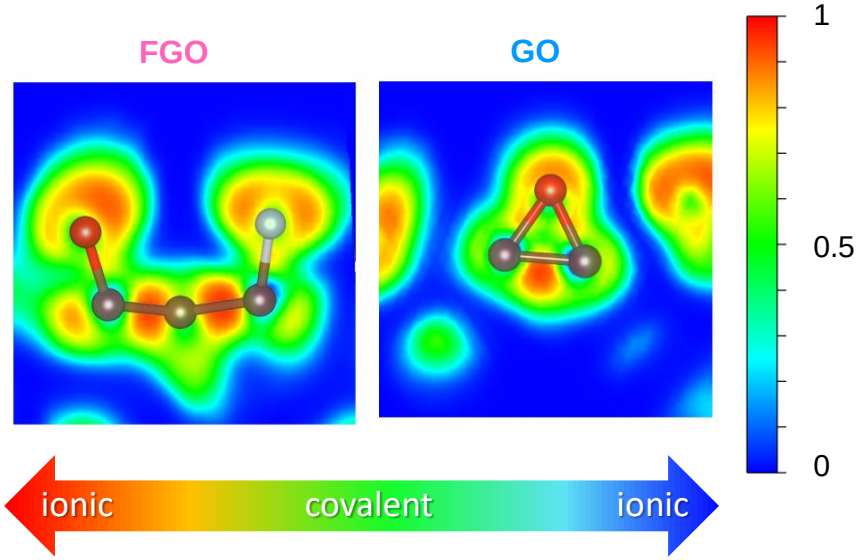

K- and OH- adsorption energies

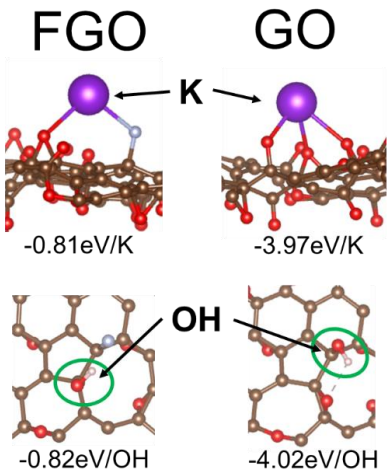

- $\Delta G_{OH} = \Delta E_H + \Delta E_{ZPE} - T\Delta S - 0.059pH$

electron DOS of FGO and GO

- FGO has electron state population just above Fermi energy, which means that higher electron can be excited with thermal energy
- FGO layer is expected to have higher electron density and conductivity than GO.

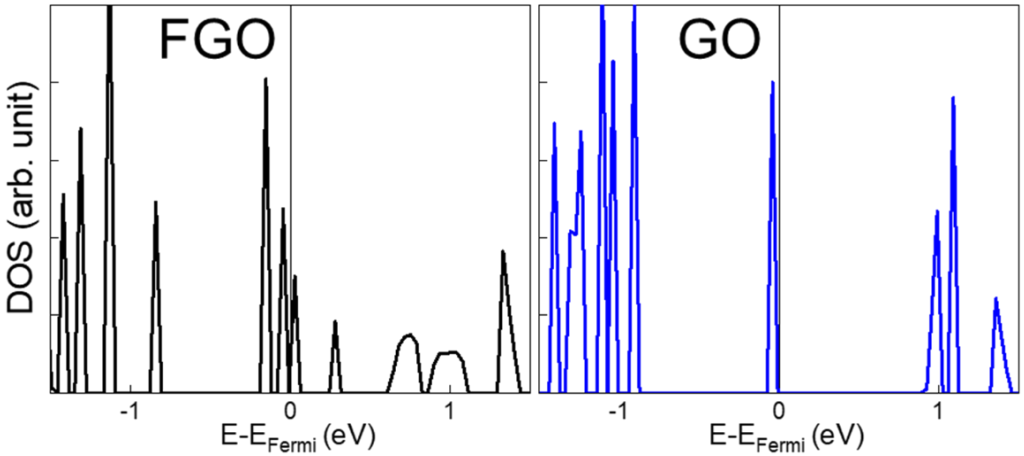

Fluorine-doped Graphene Oxide for Hybrid Supercapacitor

2-electrode device test for hybrid supercapacitor

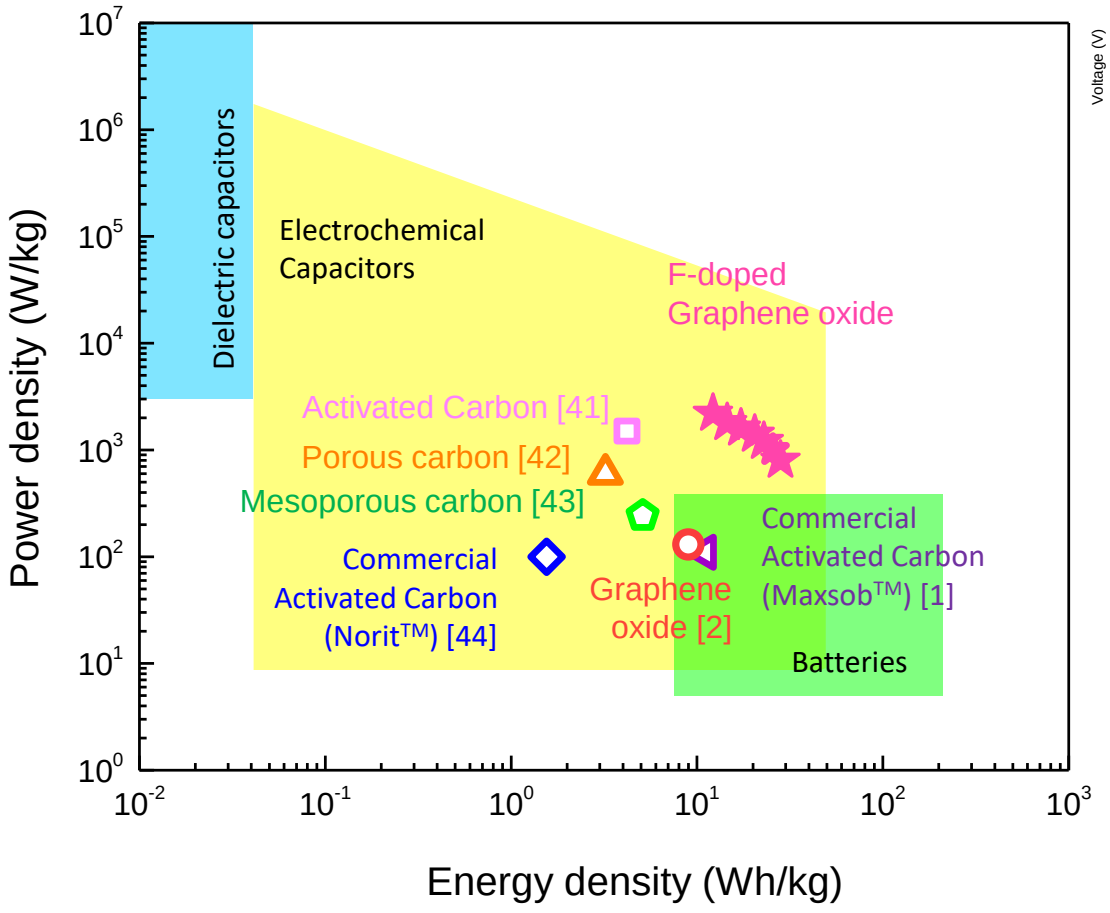

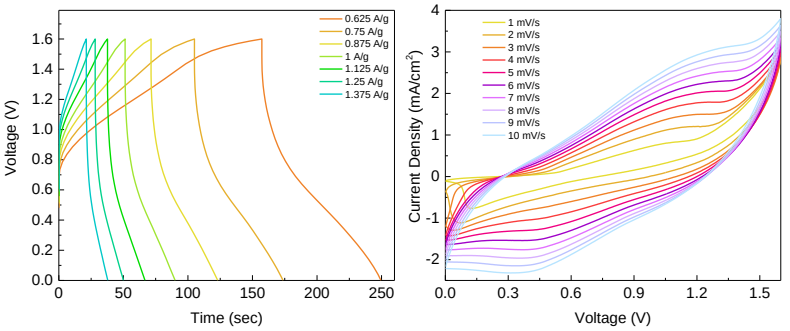

- FGO is employed as cathode and anode for hybrid supercapacitor.
- Maximum energy density of 28 Wh/kg @ 0.5 A/g
- Maximum power density of 2200 W/kg @ 1.375 A/g

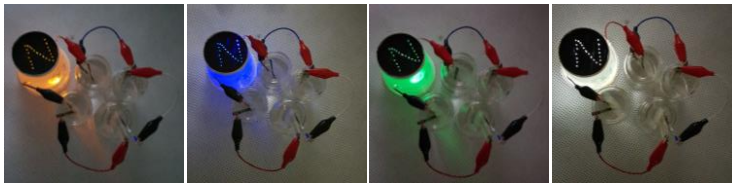

Camellia Japonica-derived Sulfur-enriched Activated Carbon

Biomass

Earch abundant

Low cost and renenue source

Industral production

Thermal treatment

Gas production

CO_2 emission

CO_2

Camellia japonica flower was applied to catalysts for operating electrochemical reactions without emission of CO_2.

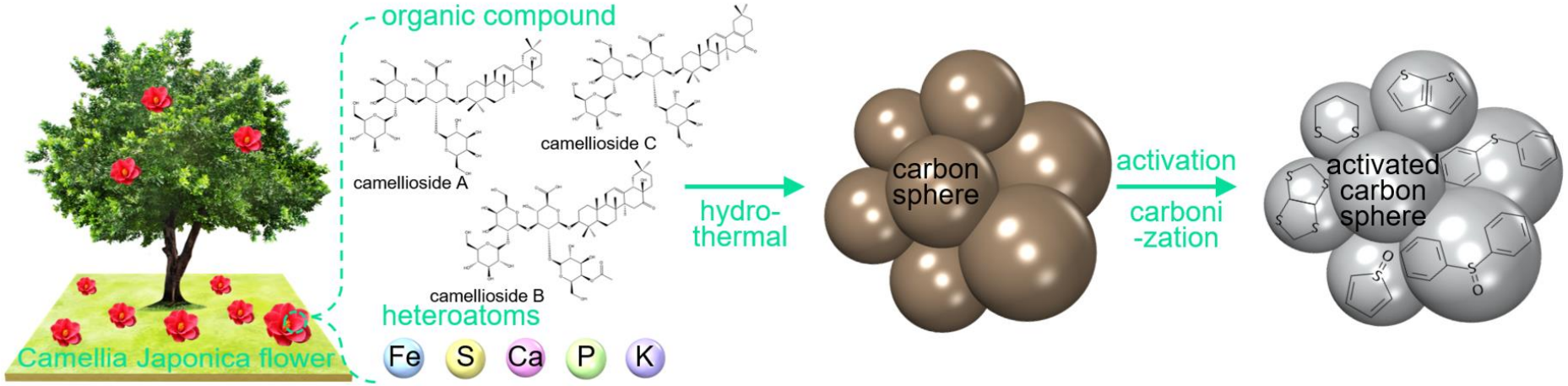

it was carbonized at the temperature of 800 ℃ for 2 h in a horizontal tube furnace at the N2 atmosphere, in which the heating rate was 5 ℃ min^{-1}, then, the obtained sample was denoted as $S\text{-}AC_{camellia}$.

Camellia Japonica-derived Sulfur-enriched Activated Carbon

Field emission scanning electron microscopy (FE-SEM)

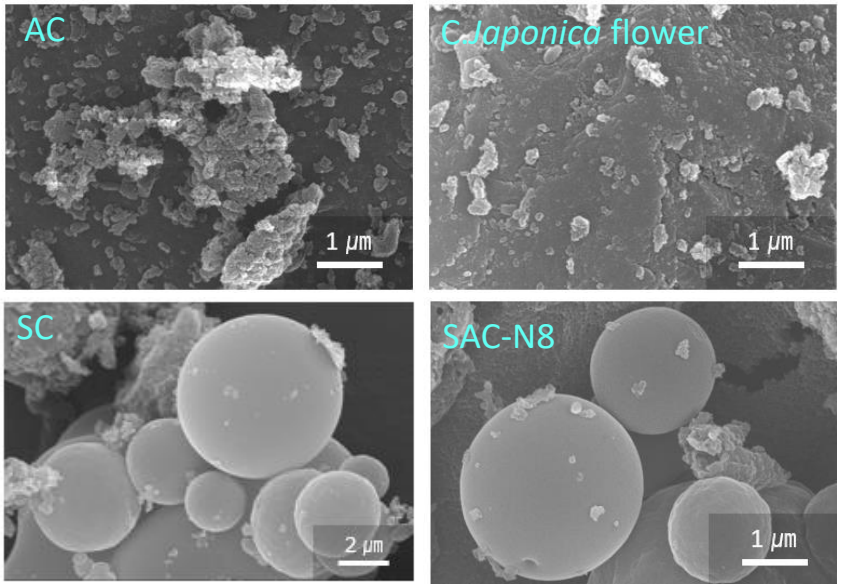

Transmission electron microscopy (TEM)

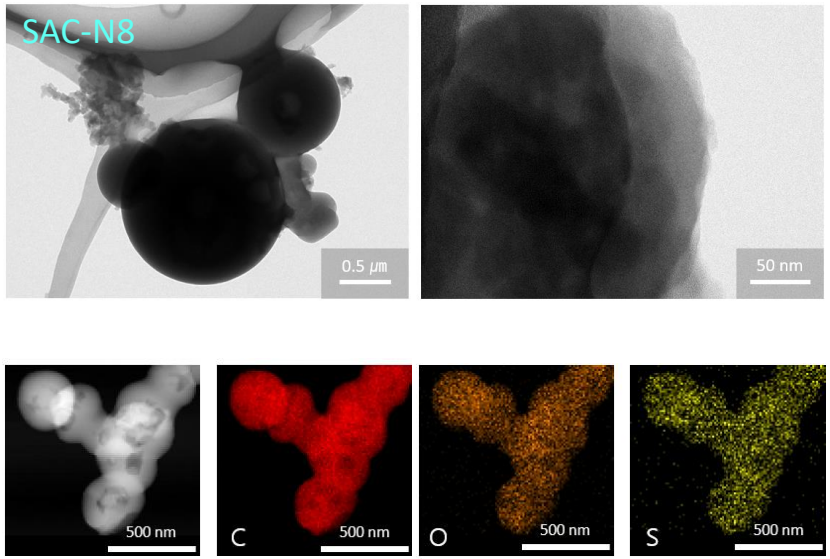

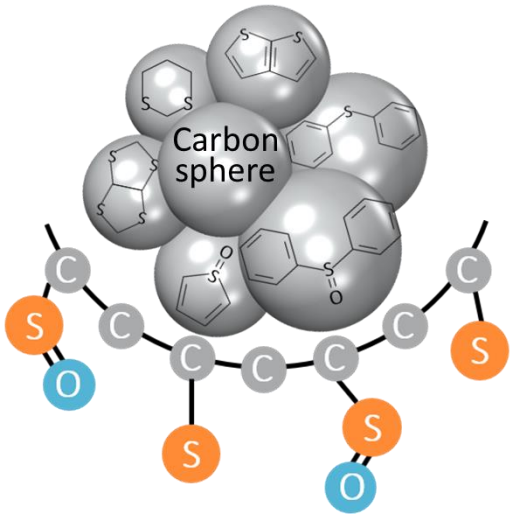

- Raw materials of C. Japonica flower and the AC show the agglomerated morphology.
- SC and SAC-N8 exhibit microsphere morphology supporting the movement of ions by providing abundant sites, moreover, morphology of SAC-N8 illustrate more defective surface than SC.
- Morover, the SAC-N8 indicates elements of C, O, and S corresponding to naturally incorporation of sulfur into the carbon structure.

AC: commercial activated carbon
SC: before activation and carbonization of the SAC
SAC-N8: sulfur-doped activated carbon carbonized at N_2 atmosphere, 800°C.

Camellia Japonica-derived Sulfur-enriched Activated Carbon

X-ray diffraction (XRD)

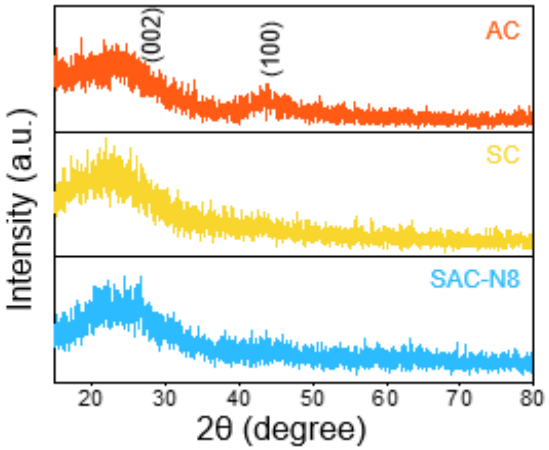

Raman spectra

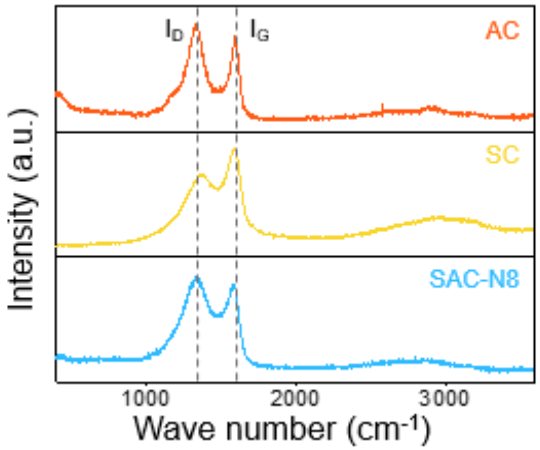

(002) plane ~ 23°: graphitic carbon
(100) Plane ~ 44°: non-graphitized carbon

- I_D/I_G: the ratio of intensity at D and G band

	I_D	I_G	I_D/I_G
AC	235.76	228.34	1.03
SC	428.88	488.82	0.88
SAC-N8	228.91	227.39	1.01

Fourier transform infrared (FT-IR)

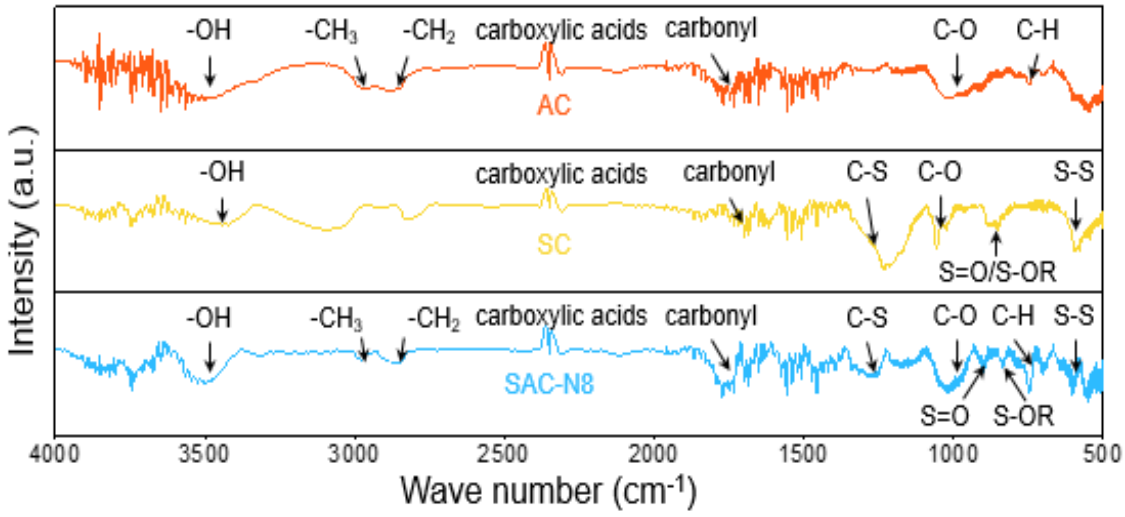

- FT-IR analysis indicates large surface functional groups of S-$AC_{camellia}$.

OH	CH_3	CH_2	carboxylic acids	
3494.9	2972.8	2861.1	2363.5	2338.9
3494.9	2972.8	2861.1	2363.5	2338.9

carbonyl	C=O	C-S	C-O-C	C-O
1764.4	1557.8	N/A	1161.8	1011.2
1764.4	1557.8	1277.7	1161.8	1011.2

S=O	S-OR	C-H		S-S
N/A	N/A	748.1	695.6	N/A
901.5	838.8	748.1	695.6	601.6

Camellia Japonica-derived Sulfur-enriched Activated Carbon

X-ray photoelectron spectroscopy (XPS)

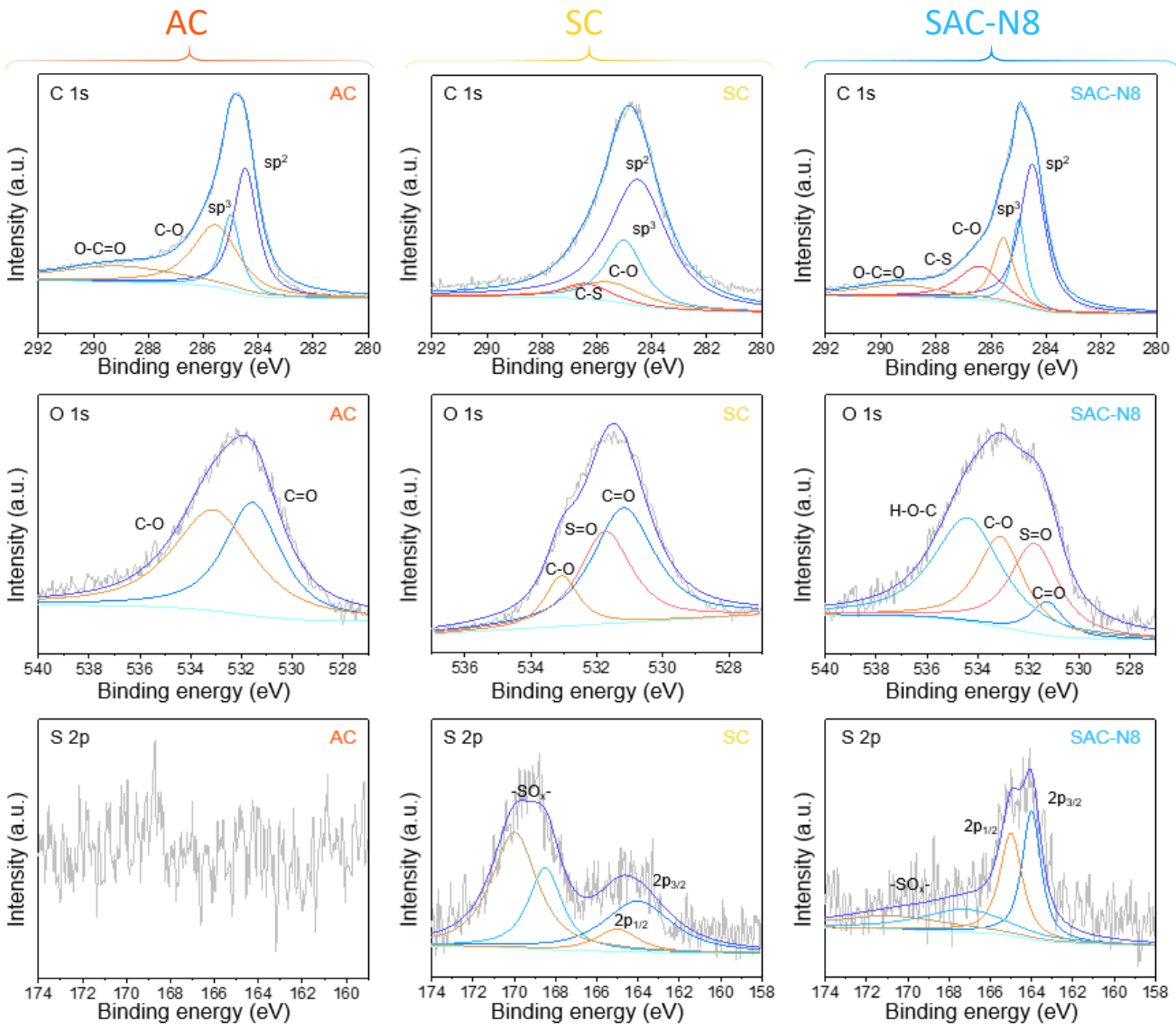

	C 1s (at. %)	O 1s (at. %)	S 2p (at. %)
AC	91.08	8.92	N/A
SC	68.58	26.4	5.02
SAC-N8	89.87	9.19	0.94

- The S-AC exhibits more oxygen groups relating to enhanced electrode wettability and more activation sites than the AC.

Camellia Japonica-derived Sulfur-enriched Activated Carbon

Supercapacitor performance of cyclic voltage (CV) at negative potential (0 to -1.0 V)

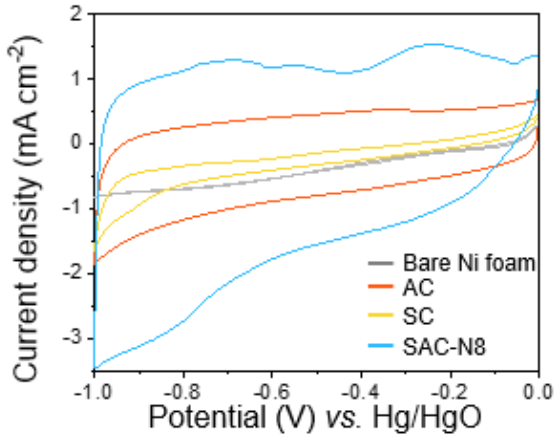

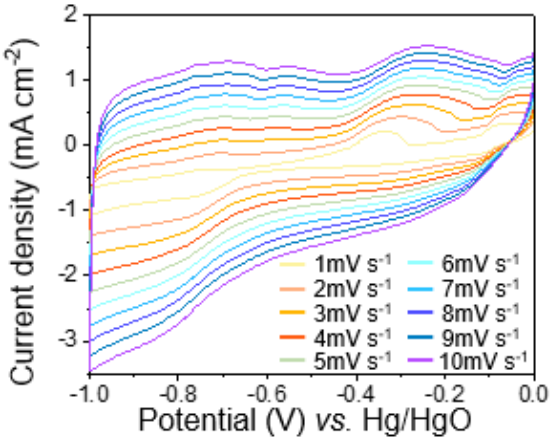

- the SAC-N8 shows a higher specific capacitance of 141.83 F g^{-1} than the AC (60.38 F g^{-1}) and bare Ni foam (0.59 F g^{-1}) from the CV curves at a scan rate of 10 mV s^{-1}.
- the SAC-N8 shows electrochemical double-layer capacitor (EDLC) behavior dominantly with several humps in the CV curves that indicate the redox reactions between the element of oxygen group and sulfur and electrolyte.

Supercapacitor performance of galvanostatic charge/discharge (GCD)

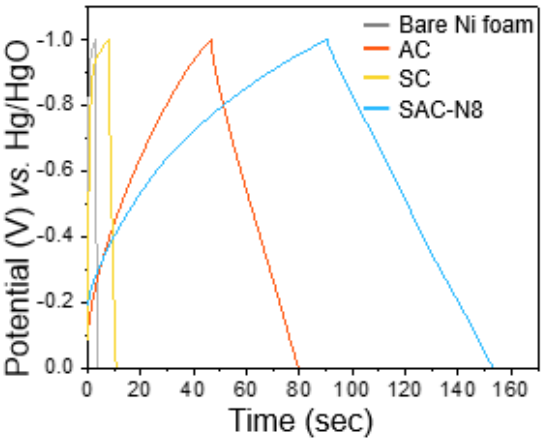

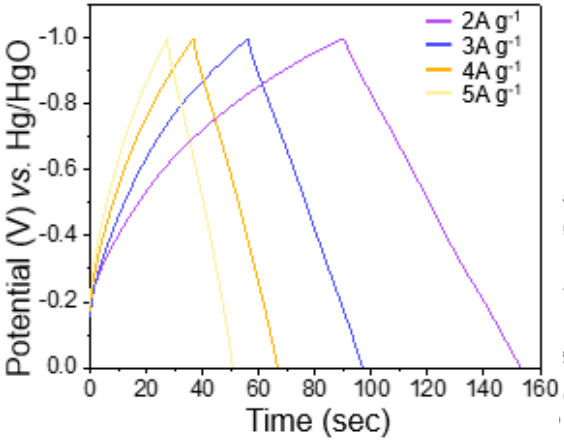

- The SAC-N8 exhibits a higher specific capacitance of 125.42 F g^{-1} than that of AC (65.75 F g^{-1}) from the GCD curve at a current density of 2 A g^{-1}.

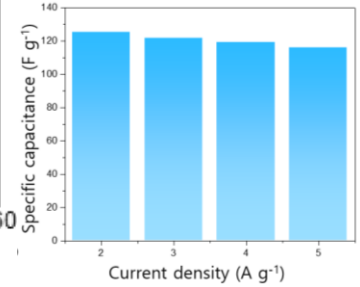

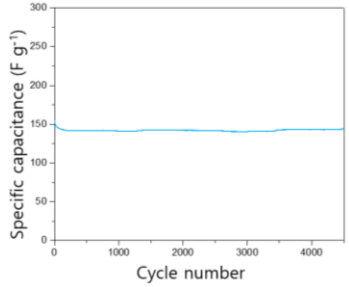

Camellia Japonica-derived Sulfur-enriched Activated Carbon

Supercapacitor performance of cyclic voltage (CV) at positive potential (0 to 0.65 V)

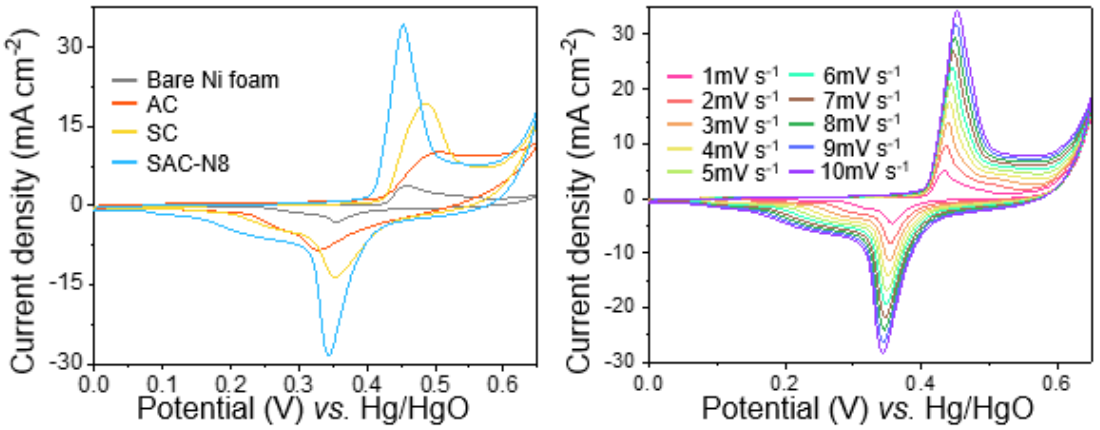

- Specific capacity of the SAC-N8 exhibits the largest value (453.85 C g^{-1}) than the AC (236.55 C g^{-1}) and bare Ni foam (61.19 C g^{-1}) from CV curve at a scan rate 10 mV s^{-1}.

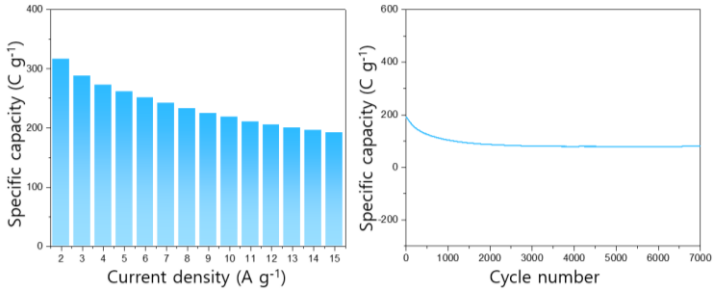

Supercapacitor performance of galvanostatic charge/discharge (GCD)

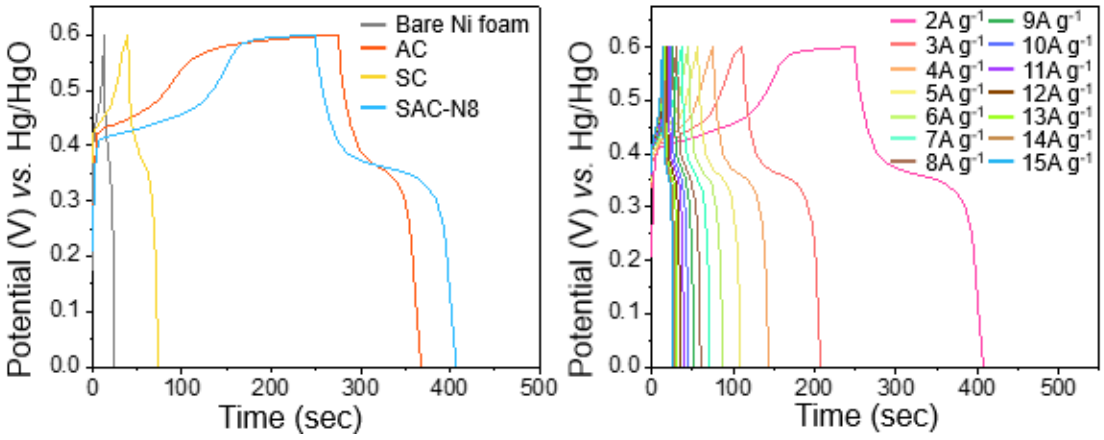

- The specific capacity of the SAC-N8 is calculated at 316.31 C g^{-1}, while that of AC is calculated 185.91 C g^{-1} from the GCD curve at a current density at 2 A g^{-1}.
- GCD curves of all samples illustrate slightly distorted triangular shape in the positive potential range due to the Faradaic redox reaction.

Camellia Japonica-derived Sulfur-enriched Activated Carbon

Supercapacitor device performance

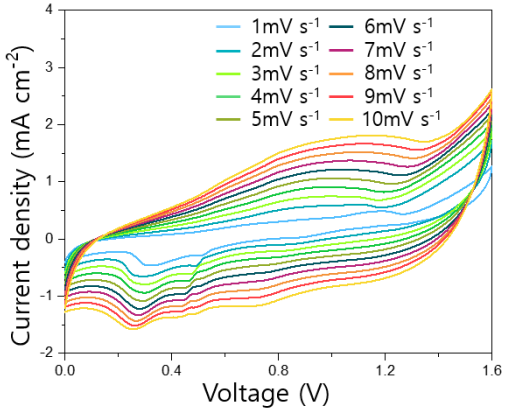

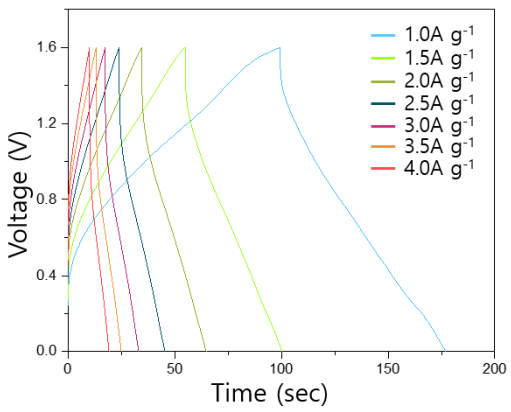

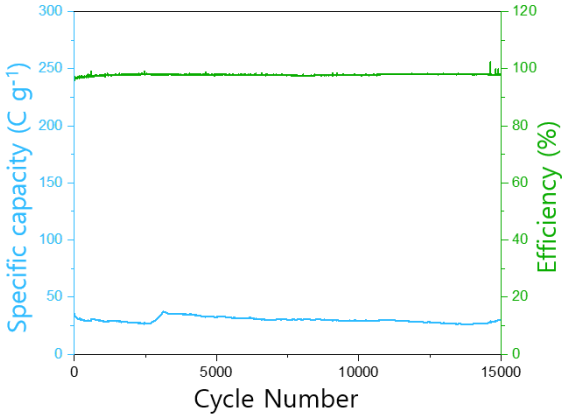

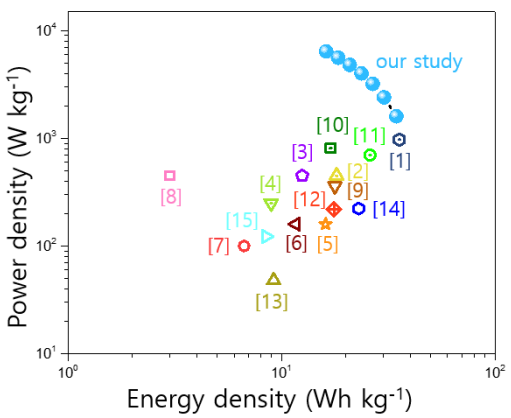

Perform to real application (LED device)

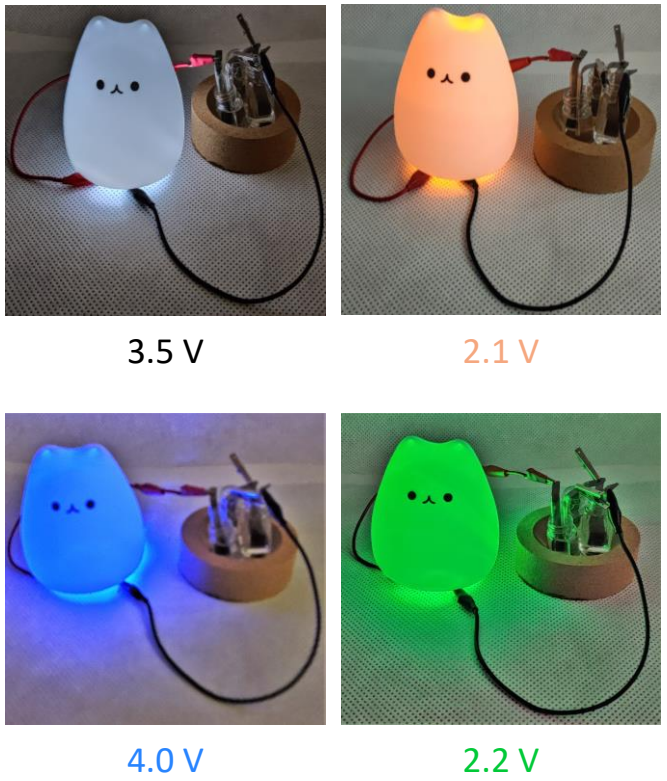

- The device stretches to a vast cell voltage of 1.6 V, which relatively higher than the reported biomass-derived devices.
- The calculated specific capacity from the CV curve shows the highest value 117.52 C g^{-1}.
- the highest energy density is improved to 34.54 Wh kg^{-1} at a power density of 1600 W kg^{-1}.

- The three-connectied device is performed for real application in the white (3.5 V), yellow (2.1 V), blue (4.0 V) and green (2.2 V) light-emitting diode (LED) devices.

Stannite-type Cu_2FeSnS_4 for supercapacitor

Morphology analysis – SEM data

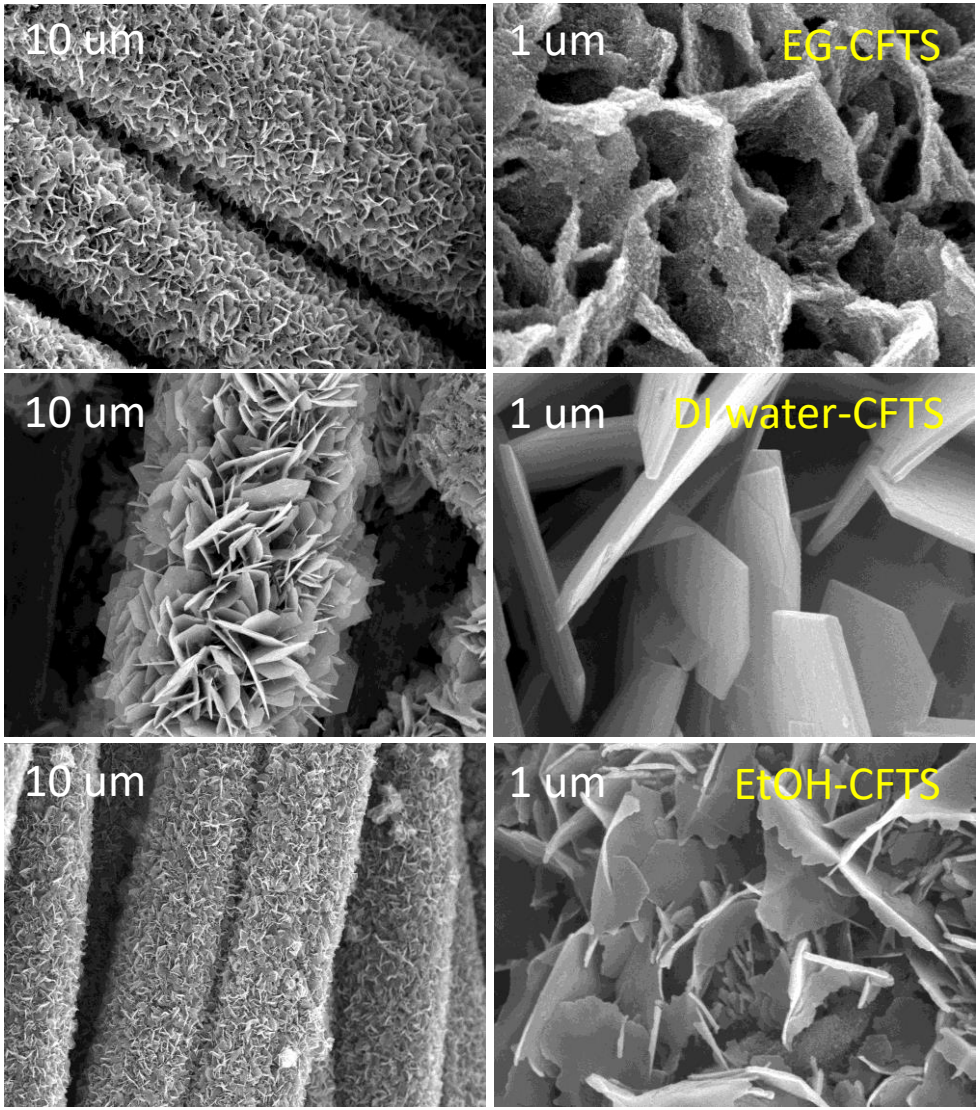

- All three samples show flake-like structures.
- The EG_CFTS shows porous rough surfaces. The rough surface can improve wettability of materials for better electron and electrolyte ion transmission.
- DI_CFTS has smooth surfaces due to the high surface capillary forces of the water solvent.
- EtOH_CFTS has smooth surface but does not have homogeneous surfaces. They promote the formation of interparticle spacing, and increase specific surface area.

XRD data

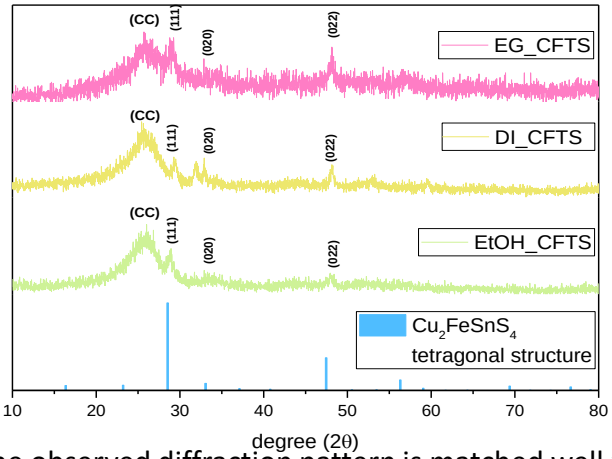

- The observed diffraction pattern is matched well with the diffraction pattern of tetragonal Cu_2FeSnS_4 phase.
- In the XRD of DI_water, we have some extra peaks between (111) and (020), that may due to phase change or presence of impurities.

Stannite-type Cu_2FeSnS_4 for supercapacitor

Morphology analysis – XPS data

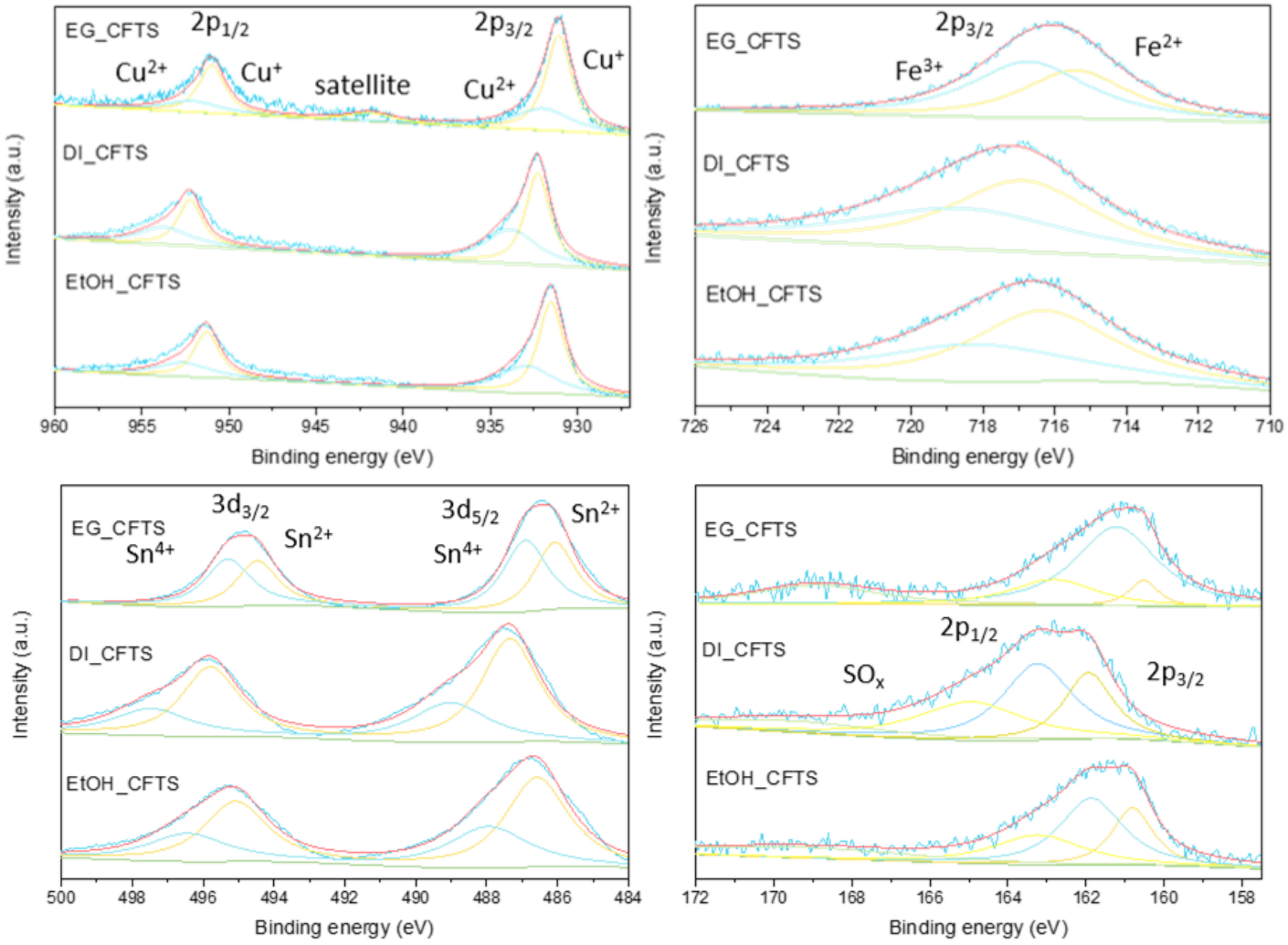

- The XPS spectra of CFTSs show the presence of Cu, Fe, Sn and S elements.
- EG_CFTS has a satellite peak and there are more active sites, which improves performance.

Stannite-type Cu_2FeSnS_4 for supercapacitor

Electrochemical data

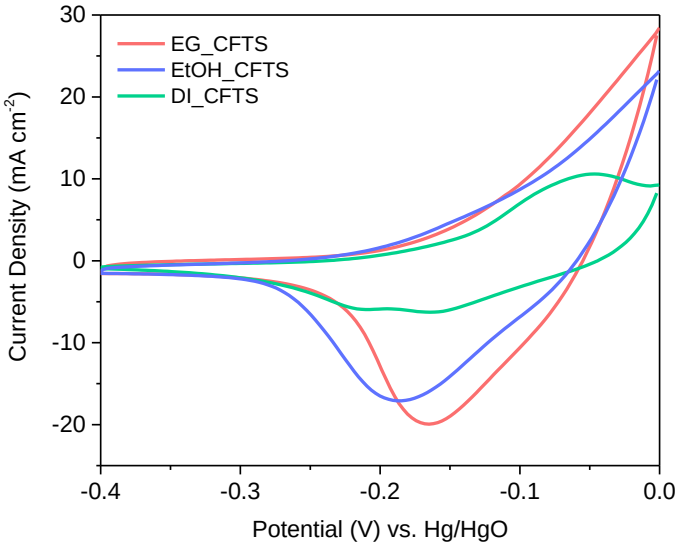

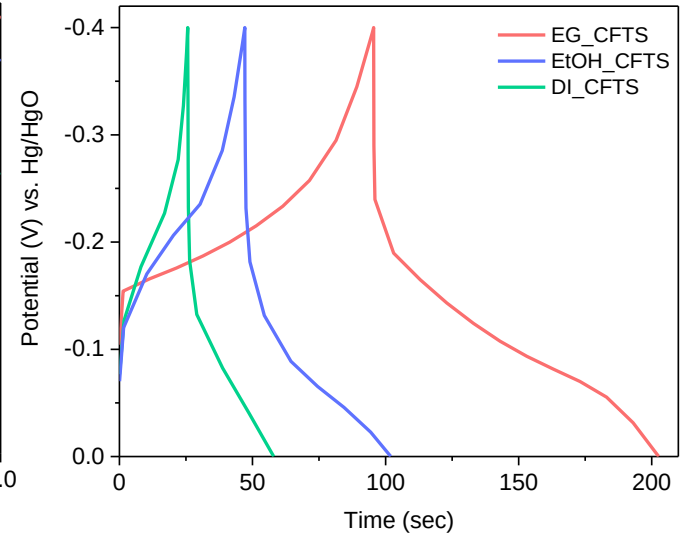

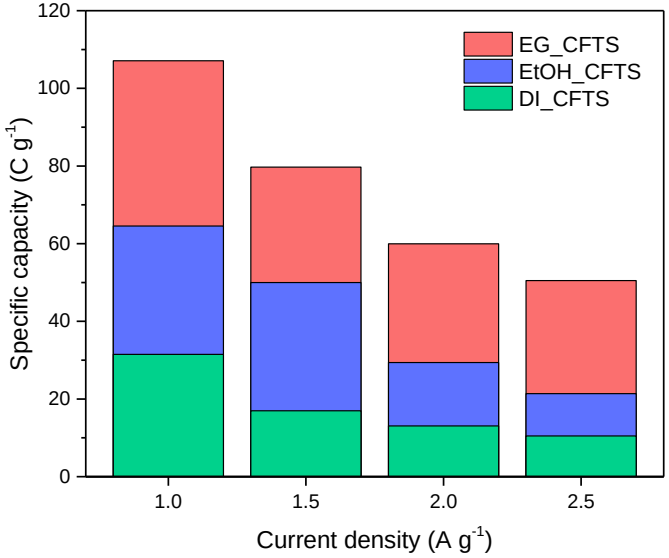

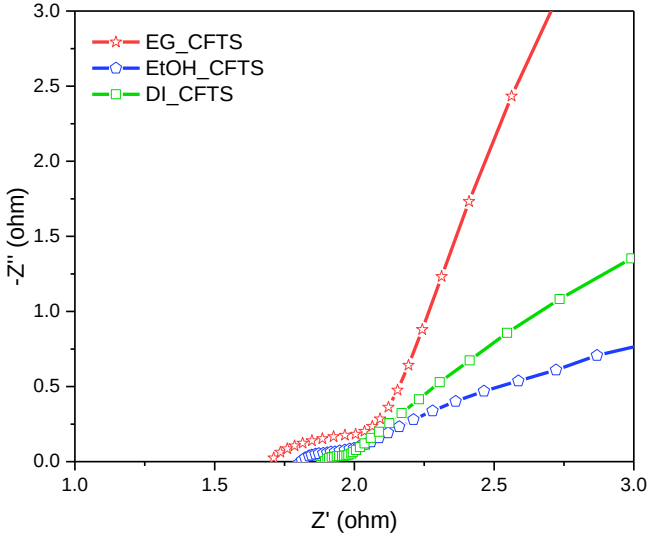

- Specific capacity of the EG_CFTS exhibits the largest value (106.11 C g^{-1}) than the DI_CFTS (23.33 C g^{-1}) and EtOH_CFTS (56.96 C g^{-1}) from CV curves at a scan rate of 10 mV s^{-1}.
- The specific capacity of EG_CFTS is calculated 107.09 C g^{-1}, while that of DI_CFTS (31.51 C g^{-1}) and EtOH_CFTS (64.55 C g^{-1}) from GCD curve at a current density of 1 A g^{-1}.
- The surface of EG_CFTS is the roughest and the most active sites, so it seems to have good performance.
- The capacity retention of EG_CFTS (47 %) is better compared to DI_CFTS (33 %) and EtOH_CFTS (33%).
- The solution resistance of EG is the lowest, so the supercapacitor performance of EG_CFTS is the best.

Co-MnO@C for Zinc-Air Battery

Preparation of Co-MnO@C

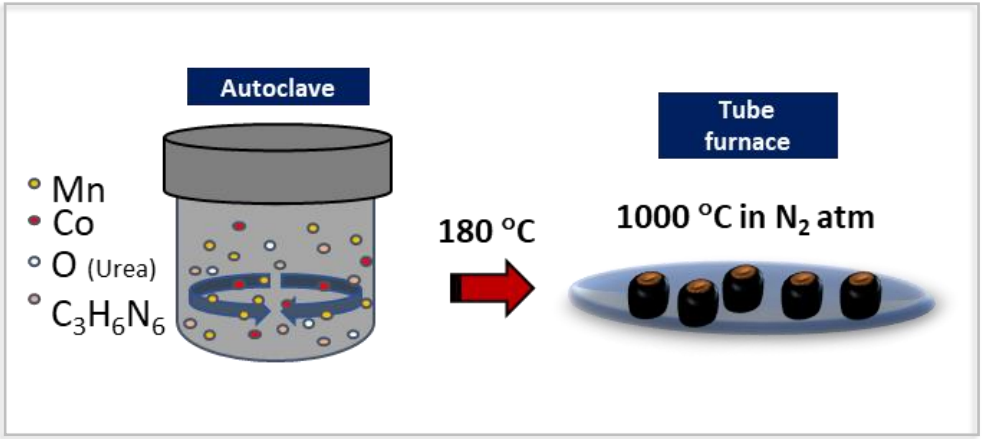

- MnO is a semiconducting oxide which can be shifted into a high valence state at a low potential in an alkaline environment where it becomes a good electron donor. This makes it an attractive candidate for the ORR.
- It is generally acknowledged that the variable valence metal ion centers of manganese oxides (MnOx) ensures good electrocatalytic activity.

Reduction of cobalt oxide

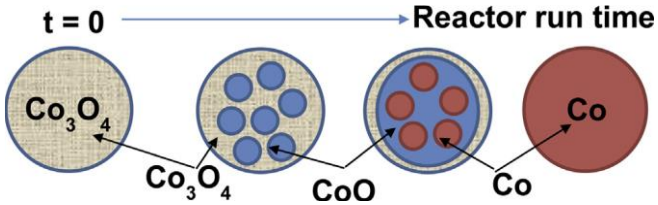

Chemical Engineering Journal, 2017, 319: 279-287.

- The pristine sample was not matched with the MnO and Co JCPDS pattern.
- After carbonizing at 350 to 450°C , the metal oxide was reduced. This can be observed in the DTA analysis.

Thermogravinetry/Differential thermal analysis (DTA)

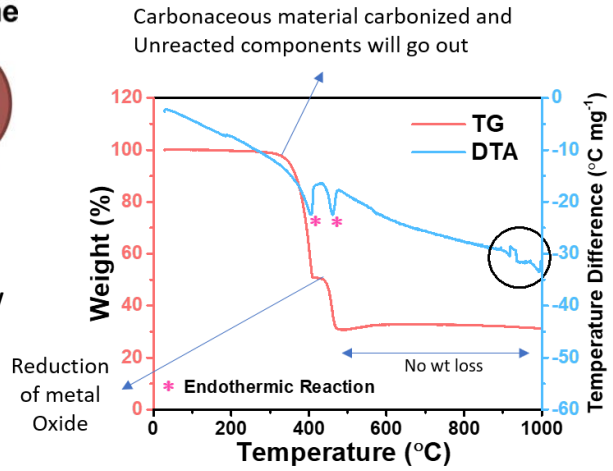

$$CoOx + C + Heat \xrightarrow[350 \text{ to } 450\ ^{o}C]{\text{Reduction}} CoO + CO_{(gas)} \quad (1)$$

$$CoO + C + Heat \xrightarrow[450 \text{ to } 500\ ^{o}C]{\text{Reduction}} Co + CO_{(gas)} \quad (2)$$

$$Mn_xO_y + C + Heat \xrightarrow[350 \text{ to } 450\ ^{o}C]{\text{Reduction}} MnO_{y-x} + CO_{(gas)} \quad (3)$$

$$MnO_{y-x} + C + Heat \xrightarrow[450 \text{ to } 500\ ^{o}C]{\text{Reduction}} MnO + CO_{(gas)} \quad (4)$$

Co-MnO@C for Zinc-Air Battery

XRD pattern

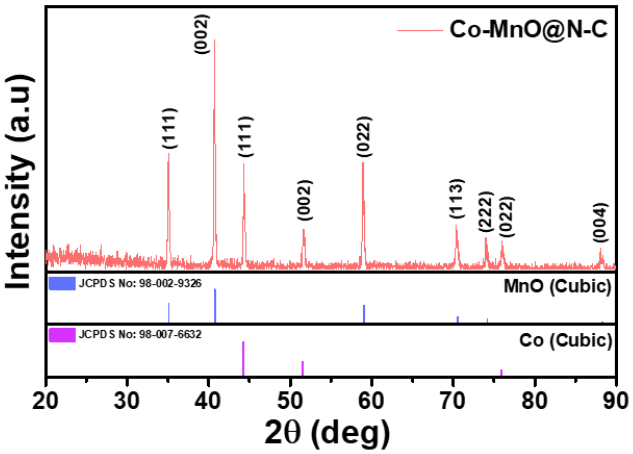

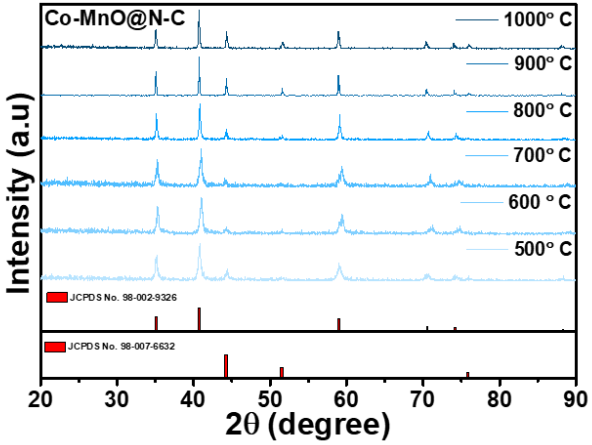

- Pristine sample was annealed at tempera tures from 500 to 1000 ^{o}C.
- As the temperature was increasing the cr ystallinity of the material was increased.
- Annealed sample matched with the MnO and Co JCPDS pattern.
- The planes of (002) and (111) for MnO a nd Co corresponds to the Cubic crystal st ructure. This crystal structure is highly el ectrocatalytic on comparing the others.

XPS analysis

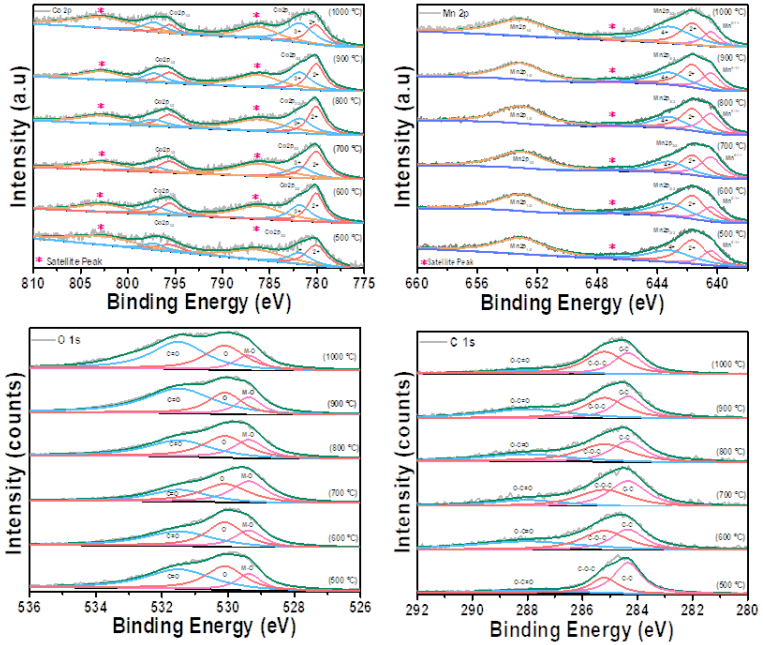

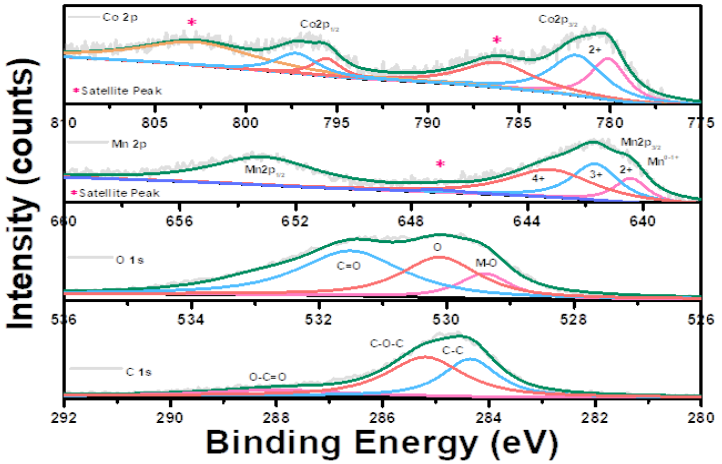

- Presence of Co, Mn, O and C was confirmed from the XPS analysis.
- Co metal at the surface was partially surface oxidized.

Co-MnO@C for Zinc-Air Battery

Temperature dependent FESEM

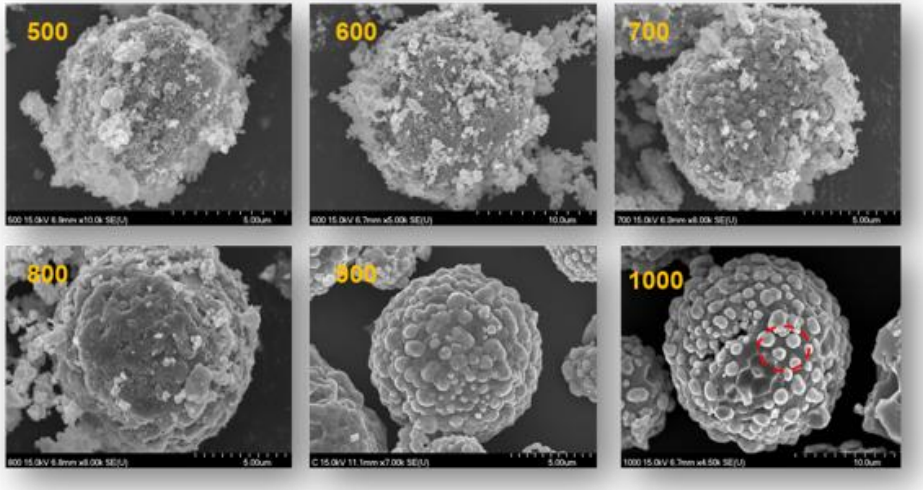

- Recrystallization is defined as the process in which grains of a crystal structure come in a new structure or new cryst al shape.
- The rate of the microscopic mechanisms controlling the n ucleation and growth of recrystallized grains depend on th e annealing temperature.
- Arrhenius equation gives the dependence of the rate cons tant of a chemical reaction on the absolute temperature, a pre-exponential factor and other constants of the reacti on.
- As the temperature increases from 500 to 1000^{o}C the crystals fuse together and form Corona- like morphology.

900 ^{o}C

1000 ^{o}C

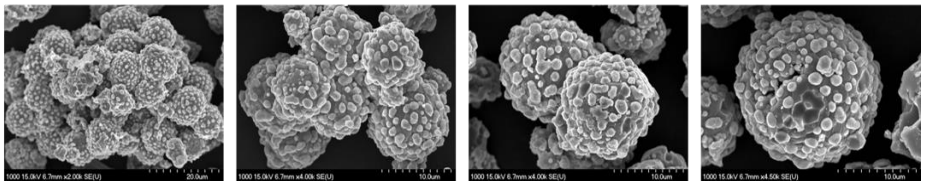

- Co-MnO@C prepared at 1000^{o}C has prominent bubbles o n the sphere.
- As the temperature increases from 500 to 1000^{o}C the crys tals fuse together and form Corona-like morphology.
- The oxygen bonded with the Cobalt evolves out as oxygen gas at high temperature gives Metallic Co islands.
- Results from bulk (p-XRD) and surface (XPS) analysis sugge st that a restructuring of the CoO phase occurs during rea ction, pushing lattice oxygen molecules from the particle bulk to the particle surface, thereby maintaining the surfa ce at a higher average oxidation state than the bulk.

Co-MnO@C for Zinc-Air Battery

HAADF TEM

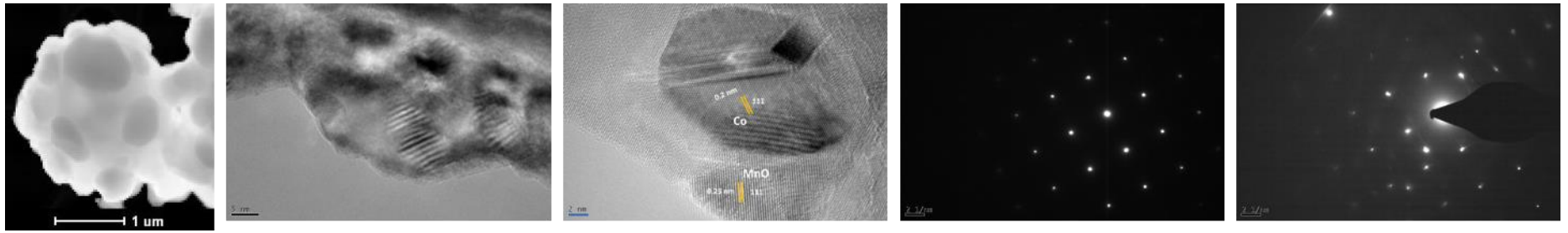

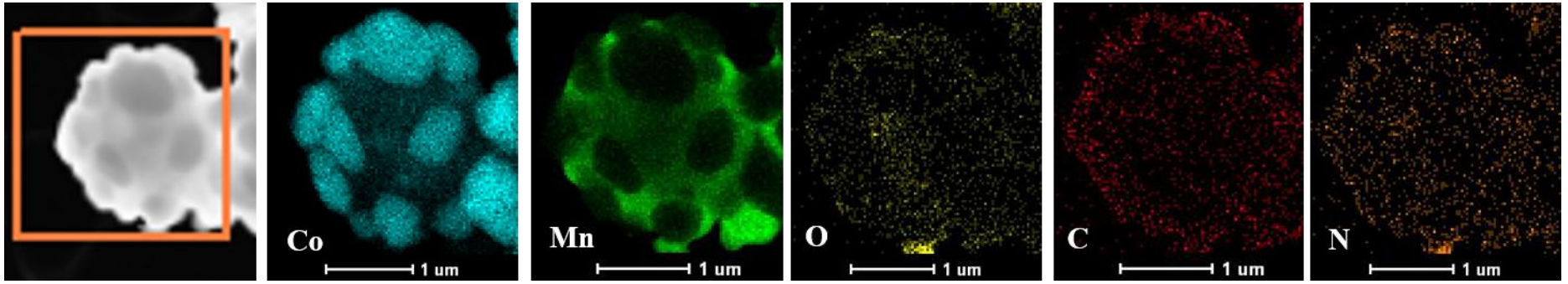

- The presence of metallic Cobalt is consistent with the TEM images.
- SAED pattern- Co-MnO@C (1000^{o}C) exhibits defined crystal lattice fringes with an interplanar spaci ng of 0.2 nm and 0.25 nm, corresponding to the (111) planes of metallic Co and (111) planes of Mn O.
- Diffraction pattern shows the crystalline nature of material.
- EDX mapping results indicated that the metallic Co is decorated on MnO.

Co-MnO@C for Zinc-Air Battery

ZAB test

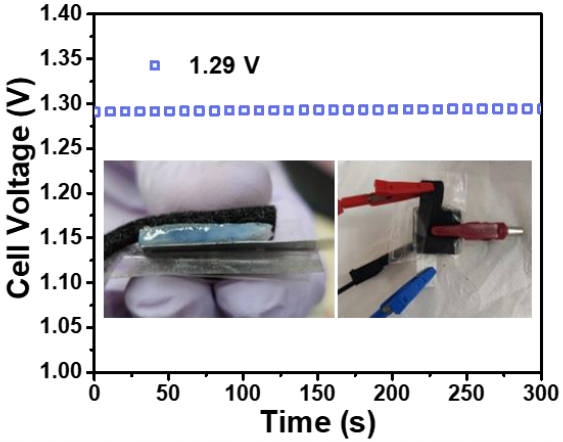

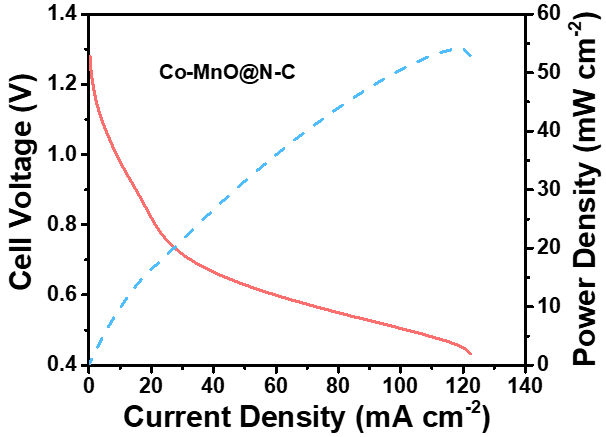

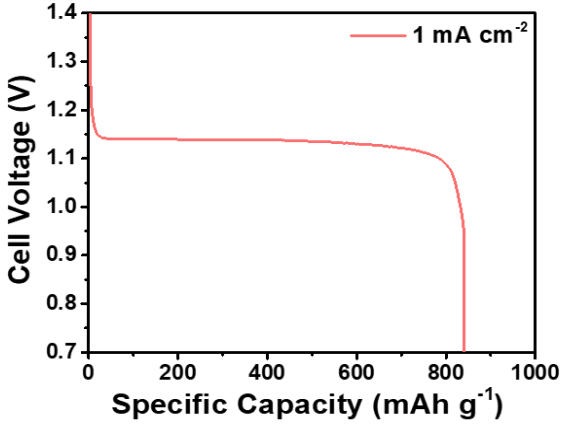

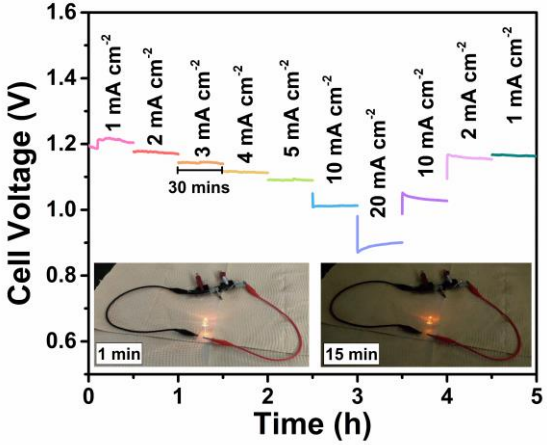

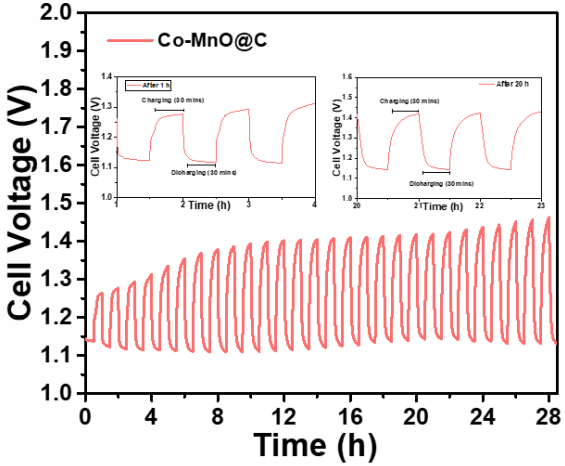

Electrocatalyst	OCV (V)	Specific capacity (mAhg-1)	Power density (mW cm-2)
Co3O4 nanopolyhedron /N-rGO	1.51	786	118
3D ordered porous Co3O4	1.36	_	_
Hierarchical nanostructured NiCo2O4	1.45	580	_
Co3O4/N-doped graphene	1.25	590	190
CuPt-NC	1.3	560	250
Co–N, B–CSs	_	641	100
SA–Fe/NG	_	_	91
Nanoporous carbon fiber films	1.48	740	185
Fe–Nx–C	_	641	96.4
Co3O4 mesoporous nanowire arrays	1.3	98.1	32
This work Co-MnO@C (1000°C)	1.29	845	55

- OCV, power density and voltage gap in C-D cycles can be improved by decreasing the thickness of the PGE.
- Efficiency of ZAB was tested with LED for 15 minutes.
- This type of ZAB can be used as the foldable energy storage device.